

On the structure and dynamics of Ellerman bombs

Detailed study of three events and modelling of $H\alpha$

N. Bello González¹, S. Danilovic², and F. Kneer³

¹ Kiepenheuer-Institut für Sonnenphysik, Schöneckstr. 6, 79104 Freiburg, Germany
e-mail: nbello@kis.uni-freiburg.de

² Max-Planck-Institut für Sonnensystemforschung, Max-Planck-Str. 2, 37191 Katlenburg-Lindau, Germany
e-mail: danilovic@mps.mpg.de

³ Institut für Astrophysik, Friedrich-Hund-Platz 1, 37077 Göttingen, Germany
e-mail: kneer@astro.physik.uni-goettingen.de

Received 3 April 2013 / Accepted 6 July 2013

ABSTRACT

Aims. We study the structure and dynamics of three Ellerman bombs (EBs) observed in an evolving active region.

Methods. The active region NOAA 11271 was observed with the Vacuum Tower Telescope at Observatorio del Teide/Tenerife on August 18, 2011. We used the two-dimensional Triple Etalon SOLar Spectrometer (TESOS) to obtain time sequences of the active region and of EBs in $H\alpha$ at a cadence of 15 s. Simultaneously, we obtained full Stokes profiles with the Tenerife Infrared Polarimeter (TIP II) in the two magnetically sensitive Fe I infrared lines (IR) at 1.56μ , scanning spatial sections of the area with cadences of 28–46 s. The $H\alpha$ data were reconstructed with speckle methods to study the evolution of the atmospheric stratification. Two methods were used to extract magnetic field information from the IR Stokes profiles: 1) fitting of the (Q, U, V) profiles by Gaussians; and 2) applying the Milne-Eddington approximation, assuming two separate magnetic structures in the resolution element and fitting by trial and error some profiles from the EB areas. Data from SDO-HMI and -AIA were also used. We performed two-dimensional (2D) non-LTE radiative transfer calculations of $H\alpha$ in parameterised models of EBs.

Results. The three EBs studied in detail occurred in a complex active region near sunspots. They were very bright with a factor of 1.5–2.8 brighter than the nearby area. They lived for 1/2 h and longer. They were related to broadband faculae, but the latter were not the brightest features in the field of view. The EBs occurred in magnetic field configurations with opposite polarity close together. One EB was located at the outskirts of a penumbra of a complex sunspot and showed repeated “flaring” in SDO-AIA data. Another was close to a strong field patch and moved into this during the end of its lifetime. The third EB showed clear changes of field structure during the time it was observed. We obtained from the 2D modelling that heating and increase in $H\alpha$ opacity are likely to occur at heights of 300–800 km. Line shifts and asymmetries can well be reproduced by velocities at these heights and also at much larger heights.

Conclusions. The three EBs occurred at sites with magnetic fields of opposite polarity, which were likely the cause of the $H\alpha$ brightening upon reconnection.

Key words. Sun: faculae, plagues – magnetic reconnection – techniques: high angular resolution – Sun: activity – techniques: polarimetric

1. Introduction

Evolving active regions (ARs) of the Sun, when observed in hydrogen Balmer lines, show conspicuous, short-duration brightenings, known as the Ellerman bombs (EBs, [Ellerman 1917](#)). As found in studies during the past six decades, EBs are small-scale structures with a size of the order of $1''$ and occur in especially complex and developing ARs and between spots. Their lifetime is reported to be in the range of a few min to $\sim 1/2$ h. EBs are especially well seen in both wings of the $H\alpha$ line from approximately $1/2 \text{ \AA}$ on outward of line centre, while the inner $H\alpha$ core is not affected. [Severny \(1956\)](#) and coworkers had seen in spectral lines “very thin brilliant wings”, extending out up to 15 \AA . From their characteristic appearance in negatives of photographic spectrograms, they called them “moustaches”. The moustaches, when seen in the Balmer lines, are likely caused by the same mechanism as the EBs, which exhibit the same extended wing brightenings. According to the studies of [Bruzek \(1968\)](#), EBs occur at all active stages of ARs but are absent

around old, unipolar spots. An overview of the extended literature can be found in the review by [Rutten et al. \(2013\)](#).

We discuss only a few recent studies here to introduce our present investigation. [Qiu et al. \(2000\)](#) analysed time sequences of EBs in $H\alpha$ filtergrams with a cadence of 0.1 s and in 1600 \AA continuum images with cadences of 1–30 s. EB intensities show a fast rise and decay, fluctuations on timescales of a few min, and eventual recurrence. The bright EBs in their sample exhibited a good correlation in $H\alpha$ and UV continuum. [Georgoulis et al. \(2002\)](#) analysed 3.5 h long time sequences with high spatial resolution ($0'.5\text{--}0'.8$) of vector magnetograms at 3.5 min cadences, of Dopplergrams and $H\alpha$ wing filtergrams, where both were taken at cadence of 7.5 min, and of TRACE data at 1600 \AA . Like [Qiu et al. \(2000\)](#), they identified many EBs with a brightness of 5–30% above the background. They found EBs at the following locations: 1) boundaries of a supergranular cell near the trailer (or f) sunspot; 2) polarity reversal in the AR with intense flux emergence; and 3) an area with newly emerged magnetic fields near the leading sunspot. Neutral lines of photospheric

magnetic fields do not appear as a prerequisite for EB triggering. Georgoulis et al. (2002) suggested several magnetic field topologies in emerging flux regions for EBs: 1) Reconnection at the top of \cup loops in converging flows or above moving dipolar features. The field lines at the bottom of the \cup loops are tangential to the solar surface, and these areas are called bald patches (BPs). 2) Quasi-separatrix layers (QSLs), defined as the layers separating systems of flux bundles connecting to different footings. The vector magnetograms from the Georgoulis et al. observations were used by Pariat et al. (2004) for extrapolation into the chromosphere and corona. They confirmed the BPs as possible sites above which reconnection can take place.

In a proceeding study, employing multi-wavelength imaging and magnetometry from space and ground with cadences of 35 s (1600 Å) to 6 min (Ca II 8542 Å and Na D₁), Pariat et al. (2007) confirmed the BP – EB relation. They also found intensity fluctuations of EBs on timescales of a few min.

Matsumoto et al. (2008) carried out observations in Ca II H and of 6302 Stokes (I, V) with HINODE/SOT at a cadence of 6 min and took simultaneous $H\alpha$ filtergrams with the Hida solar telescope at a cadence of 7 min. They found magnetic dipoles close to an EB and a substructure in EBs that is seen in Ca II H as a core and a halo. They suggested a scenario that the core is formed close to the reconnection site, while the halo consists of gas in magnetic fibrils in the surrounding. Using $H\alpha$ filtergrams and vector magnetograms from Hida observatory, Watanabe et al. (2008) found EBs in areas of undulatory magnetic fields of emerging flux regions. They suggested three different field topologies in which EBs are triggered: 1) at the foot point of converging magnetic fields of opposite polarity; 2) above BPs; and 3) in QSLs. A photometric analysis of EBs was performed by Berlicki et al. (2010). These authors also included one-dimensional atmospheric modelling of EBs.

EB observations with very high spatial resolution were presented by Watanabe et al. (2011). Before and after their 38 min filtergraph sequence of $H\alpha$ at 6 s cadence, polarimetric measurements in 6302 Å were performed. The authors suggested that they provide morphological evidence of field reconnection deep in the photosphere from their study of EB dynamics in $H\alpha$ and from the locations of EB occurrence in the AR. A study of the chromosphere above sunspots by means of scans of narrowband filtergrams across the Ca II 8542 Å line and of simultaneous Ca II H filtergrams was recently performed by Reardon et al. (2013). They found penumbral brightenings in the wing of the IR line that lasted 5–8 min and occurred simultaneously with brightenings in the Ca H filtergrams. From the wavelength position of intensity enhancement in the IR line around ± 0.4 Å off line minimum, Reardon et al. (2013) pointed out the reminiscence with the $H\alpha$ profiles from moustaches or EBs and concluded that the phenomenon is caused by heating in the temperature minimum region. Recently, Nelson et al. (2013) also presented a statistical analysis of EBs near a sunspot, although of low contrast in the wing of $H\alpha$ with intensities a factor of ≤ 1.3 above average. They found that EBs can be very small, $< 0''.3$, and short-lived, with lifetimes < 3 min and suggested also that EBs are caused by magnetic field reconnection.

Numerical magneto-hydrodynamic simulations of flux emergence in three dimensions were carried out by Archontis & Hood (2009). They showed that field reconnection occurs at various heights from sub-photosphere to chromosphere due to the non-linear and highly dynamic evolution of the system. Archontis & Hood (2009) found that reconnection occurs preferentially at locations where the magnetic field lines have a V-shape, but

also QSLs between field systems with different connectivity are sites of reconnection. The model gave density increases in the low chromosphere up to a factor of 4 and temperature enhancements by a factor of ~ 1.3 , which are close to the values estimated by Kitai (1983), Georgoulis et al. (2002), and Pariat et al. (2004) from non-local thermodynamic equilibrium (non-LTE) modelling and radiative losses. Also the lifetime and the horizontal extent of increased density and temperature in the simulations compare well with the observations.

We finally mention the work by Cheung et al. (2010). They argued that submergence into the subphotosphere of closed flux tubes, which are disconnected upon reconnection in a *cup* loop, is a means to unload magnetic fields from the mass that they carry up during emergence.

The scenario of magnetic field reconnection for EBs is widely accepted. Yet, observations with sufficiently high spatial and temporal resolution which actually demonstrate the suggested magnetic topological structures of EBs are missing. It is necessary to follow their evolution in $H\alpha$, or in another line showing the brightening, and to measure *simultaneously* their magnetic field at fast cadences.

In the present contribution, we then study the atmospheric and magnetic structure of EBs and their dynamics on the basis of these observations. We describe the observations in Sect. 2 and the data analysis in Sect. 3. The results are presented in Sect. 4. We first show the locations of the observed EBs in the AR in Sect. 4.1 and close-ups of intensities and magnetic fields in Sect. 4.2. In Sect. 4.3, we study the temporal evolution of EBs and their neighbourhood from sequences of intensities and magnetic field maps and from the evolution of IR Stokes (Q, U, V) profiles. We made attempts to find possible atmospheric structures during EBs from two-dimensional (2D) non-LTE radiative transfer in $H\alpha$. The results are reported in Sect. 4.4. Section 5 concludes this paper.

2. Observations

The data were obtained from the large, evolving AR NOAA 11271 on August 18, 2011 from 08:02 UT to 10:10 UT with the Vacuum Tower Telescope at the Observatorio del Teide/Tenerife. The spots of the AR were located at (40° – 50° E, 15° – 20° N) with an average heliocentric angle of $\theta \approx 46^\circ$ ($\mu = \cos \theta \approx 0.69$). We performed simultaneous observations of $H\alpha$ with the two-dimensional (2D) Triple Etalon Solar Spectrometer (TESOS, Kentischer et al. 1998; Tritschler et al. 2002) and magnetic field measurements in the two infrared (IR) Fe I lines at 1.565μ with the Tenerife Infrared Polarimeter (TIP II, Collados et al. 2007). The Fried parameter r_0 during the observations was in the range of 10–15 cm.

The observations were organised as follows: The image was stabilised by the Kiepenheuer Adaptive Optics System (KAOS, von der Lühe et al. 2003). A dichroic beam splitter plate fed TESOS with the visible part of the spectrum while transmitting the infrared light to the slit spectrograph of the VTT for observation with TIP.

Since we wanted to use the time with good seeing, we decided to search for ongoing EBs in the AR. For this purpose, an $H\alpha$ interference filter with FWHM of ~ 3 Å was mounted in the video channel of TESOS. This also served to assess the seeing conditions. We chose small dark structures, such as pores if possible, that were close to an EB as lock points for KAOS. The image of the selected EB was centered by means of the tip-tilt mirror of KAOS on the entrance slit of the spectrograph where TIP was mounted.

We used TESOS in a setup with a short effective focal length, F number 1/128 (von der Lühe & Kentischer 2000), which gives a light level at the detector that is higher by a factor of 4 than with $F = 1/256$ at the expense of high spatial resolution. The pixel size corresponded to $0''.175$. The narrowband channel of TESOS was equipped with an $H\alpha$ pre-filter with FWHM of 8.7 \AA . We scanned the $H\alpha$ line in a speckle imaging mode: 12 positions across the line, $\Delta\lambda = 0.203 \text{ \AA}$, 8 frames at each wavelength position, and an exposure time of 20 ms yielding a cadence of 15 s. Due to a mistake in the wavelength positioning of TESOS, the scanned range about $H\alpha$ line centre was from -0.93 \AA to $+1.30 \text{ \AA}$ instead of a symmetric range. $H\alpha$ has terrestrial H_2O blends at 0.71 \AA , 1.25 \AA , and 1.40 \AA on the red side of the average (quiet Sun) line minimum. Broadband frames were taken through a 630 nm interference filter with FWHM of 22 nm strictly simultaneously with the narrowband images.

TIP II observations of the IR Fe I lines (at $1.5648 \mu\text{m}$, Landé factor $g = 3$, and at $1.5652 \mu\text{m}$, $g_{\text{eff}} = 1.53$) were performed with scans of the solar image perpendicular to the slit with step size corresponding to $0''.7$ and a slit width of $0''.67$. The pixel size in the slit direction corresponds to $0''.179$. Scanning was from west to east. In one case, 11 image positions across the EB were chosen giving a cadence of ~ 46 s. In two other cases, measurements were performed at seven positions yielding a cadence of 28–30 s. The exposure time for TIP was 160 ms and four exposures were accumulated in each state of the polarimetric analyser. The narrow ranges of image scanning for the TIP observations were chosen to arrive at short cadences, well below 1 min.

We concentrated on the most brilliant structures seen in the ($H\alpha$) video images. They are clearly distinct and much brighter than the bright facular structures that are almost ubiquitously present in ARs and are well visible on the blue side of $H\alpha$ line centre (Leenaarts et al. 2006). The evolution of three very bright EBs was followed: EB 1 for ~ 3.3 min, EB 2 for ~ 31 min with an interruption of ~ 1.5 min, and EB 3 for ~ 26 min with an interruption of ~ 25 s. TESOS and TIP II observations of these EBs were started and stopped at the same times.

Large fields of view (FOVs) of $80''$ and $58''$ width from parts of the AR were scanned after the EB time sequences. TIP II was taking polarimetric data during the large image scans and one 2D spectrometric TESOS scan in $H\alpha$ was taken during these times. These scans, containing sunspots and pores, provided the mutual geometric scaling of the TESOS and TIP II maps. We completed the VTT observations with dark frames, flat fields moving with the pointing around quiet Sun disc centre, and TIP II calibration data.

Finally, we also used a map of the vector magnetic field from the Helioseismic and Magnetic Imager (HMI, Scherrer et al. 2012) and images from the Atmospheric Imaging Assembly (AIA, Lemen et al. 2012) aboard the Solar Dynamics Observatory (SDO)¹. The SDO/HMI map stems from August 18, 2011, 09:12 UT, which is from the same time as the present ground-based observations. The AIA images are from August 18, 2011, 07:30–09:30 UT.

3. Data analysis

3.1. $H\alpha$ data from TESOS

3.1.1. Image reconstruction and time sequences

The broadband and narrowband images from TESOS were corrected for dark offsets and flat fielded. The broadband image

¹ Courtesy of NASA/SDO and the AIA, EVE, and HMI science teams.

bursts from each time step and the corresponding scans through the $H\alpha$ line were reconstructed with the Göttingen speckle codes (de Boer 1996; Janssen 2003; Bello González et al. 2007). The resulting $H\alpha$ profiles from each temporal and spatial position were smoothed with running means with weights $[0.26, 0.48, 0.26]$ to reduce the intensity fluctuations along wavelength. These fluctuations are instrumental and occur in some Fabry-Perot spectrometers (see e.g., Bello González & Kneer 2008, Fig. 1). Then the profiles were corrected for the wavelength dependent transmission of the pre-filter.

To locate EBs, we took average images from $H\alpha$ profile positions of -0.93 , $+0.89$, $+1.1$, and $+1.3 \text{ \AA}$ off line centre. They are henceforth named $H\alpha_{\text{wing}}$ images. Furthermore, we produced images of intensities from the local line minima, of the intensities at -0.45 \AA off average line centre, of line minimum positions, and of the bisector positions, where the local intensities in both wings are those at $+0.93 \text{ \AA}$ away from average line minimum (in the case that the blue wing had a lower maximum intensity than at $+0.93 \text{ \AA}$ the positions at this intensity were chosen). The latter bisector determinations are intended to measure velocities in EBs. The intensity at -0.45 \AA roughly reflects a line shift of the profile with bright meaning motion away from the observer, which is mainly a motion of the overlying dark chromospheric fibrils.

The chromosphere of the observed region was extremely active with strong flows in extended fibrils. Figure 2 below shows snapshots from the area containing EB 2: intensities in broadband, $H\alpha_{\text{wing}}$, line minimum, and -0.45 \AA , and velocities from wing bisectors and line minimum position. The images from the $H\alpha$ line core from the areas around EB 1 and EB 3 show similar complexity. One sees that large-scale structures ($>10''$) dominate the intensity and flow patterns in most of the $H\alpha$ images. These deserve a separate investigation, such as that of magneto-dynamic waves and jets discussed in Sánchez-Andrade Nuño et al. (2008). We concentrate here on the broadband and $H\alpha_{\text{wing}}$ intensities for the present study of EBs at small scales. The broadband and $H\alpha_{\text{wing}}$ time sequences were de-stretched by taking the running mean images over 11 consecutive temporal positions as reference (e.g., November & Simon 1988). De-stretching removes residual distortions from individual reconstructed images.

3.1.2. Correction for parasitic light

Measured intensities are contaminated by parasitic light from scattering in Earth's atmosphere and by the optical components of the telescope and the post-focus instruments. The amount of parasitic light, or stray light, can be a substantial fraction of the light level. This problem was recently dealt with thoroughly by Feller (in prep.) for the stray light correction of SUNRISE observations (Solanki et al. 2010). Sources of stray light at the 1 m Swedish Solar Telescope were investigated by Löfdahl & Scharmer (2012).

Feller (in prep.) used SUNRISE observations near the solar limb to determine the point spread function (PSF) and the level of stray light. He found three contributions with which he could reproduce the limb profile: 1) a very broad PSF, assumed constant, that is independent of spatial position, thus a Dirac δ function in Fourier space, with total contribution of 11% of the quiet Sun intensity; 2) a Gaussian with $FWHM = 0''.9$ and total contribution of 50%; and 3) another Gaussian with $FWHM = 7''.7$ and total contribution of 1.3%.

Such limb measurements are not available for the present study. Instead, we used the measured intensities in the large sunspots and pores of the observed AR and compared those with values given in the literature. The centres of large umbrae receive the stray light mainly from the wide-angle scattering, which we approximated with a constant value which is proportional to the average intensity of a nearby area free of spots and pores. The intensities of pores are contaminated in addition by a small-angle scattering component.

We adopted intensity ratios of umbra/quiet photosphere of 0.08–0.10 in the wavelength range 6000–6670 Å at $\mu = 0.69$ from Maltby et al. (1986, Table 1 and Fig. 2). For the intensity ratios of large pores with diameter 4''–5'', Sütterlin (1998, Table 3) gives a value of 0.31 at 6000 Å. These ratios were obtained for the present data in two steps. We first applied a wide-angle scattered light correction to obtain intermediate intensities according to

$$I_{\text{int}} = (I_{\text{obs}} - \alpha \bar{I}) / (1 - \alpha), \quad (1)$$

where I_{int} , I_{obs} , and \bar{I} denote the intermediate, the observed, and the average intensities, respectively. The latter is taken from a nearby undisturbed area. The stray light parameter α was chosen $\alpha = 0.12$ for both the broadband and the $H\alpha_{\text{wing}}$ images. The second step consisted of deconvolving I_{int} with a 2D Gaussian $G(x, y, \sigma)$ normalised to $\int G(x, y, \sigma) dx dy = 1$. That is the PSF is

$$\text{PSF} = (1 - \beta) \delta(x - x_0, y - y_0) + \beta G(x - x_0, y - y_0, \sigma) \quad (2)$$

with the Dirac δ function and the co-ordinates (x_0, y_0) of the centre of the images. We also chose the narrow-angle scattering parameter $\beta = 0.12$ and a σ that gives a FWHM of the Gaussian corresponding to 7''.7. With these parameters, the umbra and pore intensity results were close to the values in the literature.

Actually, the correction for wide-angle and narrow-angle scattering should be done simultaneously in one step. The PSF should be

$$\text{PSF} = (1 - \alpha - \beta) \delta(x - x_0, y - y_0) + \alpha L(x - x_0, y - y_0) + \beta G(x - x_0, y - y_0, \sigma) \quad (3)$$

with the very broad, normalised scattering function L , although this would involve all features in the FOV including large dark sunspots. The way we proceeded allowed us to select a non-spot area to determine \bar{I} . We tested Eq. (3) for a small subfield. The difference compared with the applied method for the *rms* continuum contrast is minor with $\sim 0.5\%$ of the continuum intensity.

Stray light was also considered in recent studies (e.g., Bello González et al. 2009) to bring the granular intensity fluctuations from numerical simulations to the measured values. There a Gaussian and a constant contribution were also considered. A Lorentzian stray light function was applied in addition. These 2D Lorentzians have the problem of normalisation, because the integral from $-\infty$ to $+\infty$ in (x, y) diverges logarithmically. Here, we perform a *deconvolution* to account for the stray light. For this, the PSF in Eq. (2) is most easy to apply. See also the discussion by Schlichenmaier & Franz (2002).

Typical increases in the rms intensity contrasts, relative to the mean intensity, of non-spot and non-pore areas by the stray light correction were from 0.074 to 0.108 for the broadband images. The intensities of EBs, relative to the intensity of their surrounding, increased by typical factors of 1.2 from e.g. 1.75 to 2.1. This underlines the strong effects of scattered light. The

corrections are likely lower estimates. The true sunspot intensities in the broadband images around 6300 Å are lower than the continuum intensities given by Maltby et al. (1986) due to stronger absorption lines than in the quiet Sun and due to a haze of many molecular lines. The stray light in the narrowband images is larger than in the broadband images, because the narrowband channel of TESOS has more optical components than the broadband channel.

3.2. Infrared lines from TIP II

The TIP spectrograms also were corrected for the dark offset and flat fielded. They were not corrected for parasitic light. The calibration data gave the instrumental Mueller matrix from the VTT's prime focus to the detector. The Mueller matrix of the coelostat mirrors and the telescope proper was calculated from a telescope model (Schlichenmaier & Collados 2002). With the instrumental polarisation given, the Stokes profiles $S_\lambda = (I_\lambda, Q_\lambda, U_\lambda, V_\lambda)$ were obtained. The profiles were smoothed with a low-pass filter with $FWHM = 145 \text{ mÅ}$ and normalised to the *local* continuum. We present an example in Fig. 16 showing that the wavelength filter has little, if any, influence on the amplitudes and widths of the profiles. The noise at continuum wavelengths was $\sim 8 \times 10^{-4} I_c$, where I_c is the average continuum intensity of Stokes I outside dark features as pores or spots. Stokes I continuum intensities were determined from averages along wavelength in the continuum and line minimum intensities from the mean over 0.12 Å around the minimum of the average profile.

For a preliminary determination of the magnetic fields within the scanned areas, we used the strongly split Fe I 1.5648 μm line and followed the procedure of Khomenko et al. (2003), which is appropriate for weak lines. See also the discussions by Rabin (1992) and Lin (1995). We fitted two Gaussians with amplitude A_V corresponding to a σ component to the V profiles. The field strengths and the polarities were estimated from the separation and signs of the two Gaussians, respectively. Such a determination is limited to separations of approximately twice the Doppler width of the line, or approximately $B \geq 300 \text{ G}$. This is a result from the data analysis, which gave a minimum of $B \sim 350 \text{ G}$.

Three Gaussians were fitted to the Q and U profiles, with central amplitudes A_Q and A_U , respectively, that corresponds to the π component. The inclination γ of the magnetic field with respect to line of sight (LOS), can be estimated from

$$\frac{A_V}{\sqrt{A_Q^2 + A_U^2}} = \frac{\cos \gamma}{\sin^2 \gamma}. \quad (4)$$

Finally, the azimuth χ would be obtained from

$$A_U/A_Q = \tan(2\chi). \quad (5)$$

Equation (5) contains the well known 180° ambiguity, i.e. magnetic fields that differ only in azimuth by 180° (in the LOS reference frame) produce identical Stokes profiles. For instance the Q, U measurements do not allow us to decide whether a field with inclination of 45° with respect to the LOS is vertical or horizontal with respect to the solar surface, since the AR region was located at a heliocentric angle close to 45°. In many cases away from penumbrae and pores, we found strong fields with $B \sim 1500 \text{ G}$. They persisted for many minutes, and, during the intervals we observed the EBs, they did not show evidence of

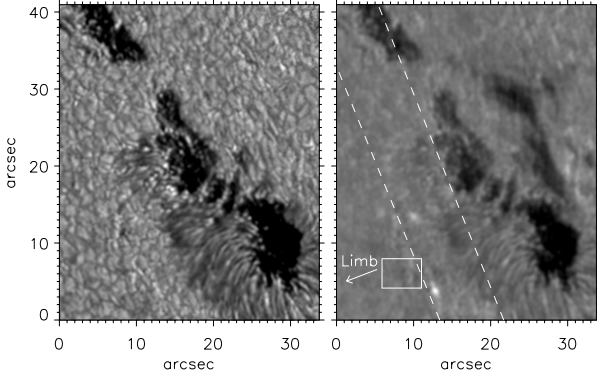


Fig. 1. Snapshot of section of AR containing EB 1. *Left panel:* broadband image; *right panel:* $H\alpha_{\text{wing}}$ narrowband image showing the EB near lower border; dashed lines: orientation of slit and scanning range for IR observations; white rectangle: area from which reference intensities for contrast measurements are taken. Direction towards solar limb is indicated by arrow. Terrestrial north is along slit towards upper border of images.

emergence of strong magnetic flux ropes with distorted granulation pattern, which were discussed by Cheung et al. (2007) on the basis of numerical simulations and comparison with observations. For these strong fields, one may assume an orientation close to the vertical due to the strong buoyancy force. We shall refrain, however, to perform a general conversion from the LOS reference frame to a local frame of reference with the vertical perpendicular to the solar surface.

Velocities along LOS were measured from the $1.5648 \mu\text{m}$ line in two ways: 1) from the Doppler shifts of the line minimum, denoted v_{lm} ; and 2) from the zero crossings of the V profiles, denoted v_{zc} . As reference for the shifts we used the average position of the line minimum for v_{lm} and of the V zero-crossings for v_{zc} , respectively.

We show in Sect. 4.3.4 that the Stokes profiles require at least two magnetic fields with different strengths and orientations within the spatial resolution element in many cases within and near EBs. This behaviour of Stokes profiles of the Fe I IR lines, e.g. with four Stokes V lobes, was already noticed by Rüedi et al. (1992) and Solanki et al. (1992) in their observations of plages and also interpreted as structures containing two fields. Thus, the determination of field strengths, inclinations, azimuths, and zero-crossing velocities that are obtained by fitting Gaussians can only give preliminary values for guidance.

4. Results

4.1. Ellerman bomb positions in AR

Figures 1 to 3 show sections of the AR under study. Terrestrial north is towards the upper borders of the images along the slit direction, as indicated by the dashed lines. Upon mirroring of light into the TESOS channel, the TESOS data are rotated with respect to the TIP II data by 22° clockwise. At the date of observation, solar north, which is also the orientation of the SDO data, was at $P = 17^\circ$, counterclockwise with respect to terrestrial north. The three EBs are seen in the $H\alpha_{\text{wing}}$ images as the brightest structures. EB 1 was only marginally covered by the scanning with TIP II. The angular resolution of the broadband images is $0'.40\text{--}0'.45$, while the narrowband images have a resolution of $0'.6\text{--}0'.8$.

The three EBs studied here are elongated and often show a substructure along their temporal evolution. This is best seen at

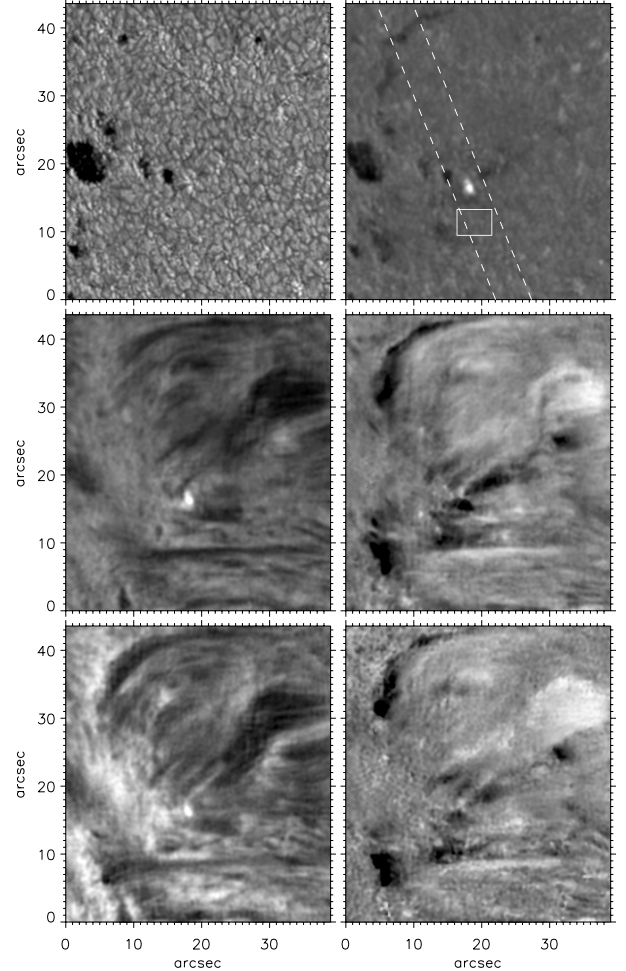


Fig. 2. *Upper row:* as Fig. 1 for EB 2; *middle row left:* intensity at -0.45 \AA off line centre of average profile; *middle row right:* velocity measured from bisectors at wing positions where EB contrast is brightest (see text); *lower row left:* line minimum intensity; *lower row right:* velocity from line minimum position, limb direction and terrestrial north same as in Fig. 1.

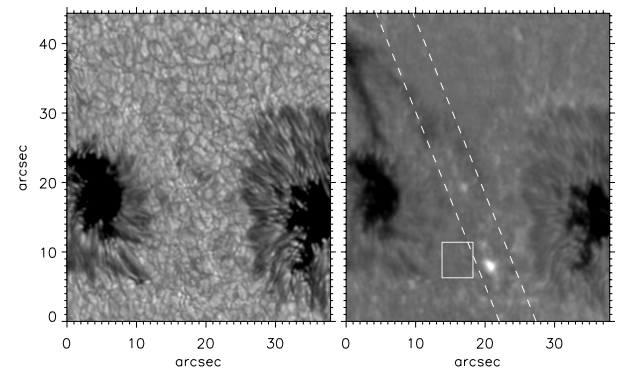


Fig. 3. As Fig. 1 for EB 3, limb direction and terrestrial north same as in Fig. 1.

EB 2 in Fig. 2, which exhibits two kernels. This EB shows a rare case where the EB was visible through the whole $H\alpha$ profile, from wing to line minimum.

We present a section of the magnetic field map of the same AR NOAA 11271 obtained from SDO/HMI observations in Fig. 4. The magnetic field strengths and the inversion lines

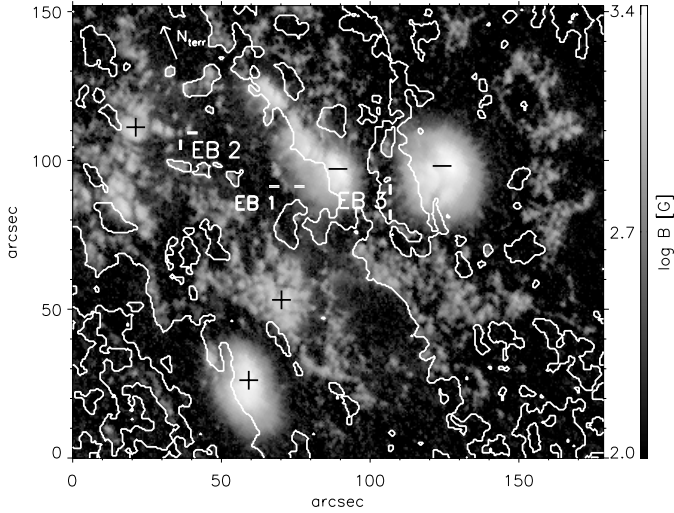


Fig. 4. Context map of magnetic field strength from inversion of SDO/HMI data taken from same AR on August 18, 2011 at 09:12 UT. Sites of three EBs under study are marked by short white double lines, direction of terrestrial north is given by arrow (upper left corner). Solar north is $17^\circ (=P)$ counterclockwise to terrestrial north. Black “+” and “-” signs give field polarity, white contours outline inversions of field polarity in LOS reference frame.

(white contours in LOS reference frame) were obtained from maps made available by the SDO/HMI team after inversion of full Stokes measurements with the code by Borrero et al. (2011). The map was rotated to the same orientation as Figs. 1 to 3. The sites of the EBs are marked in Fig. 4. The fields reach values up to $B = 2700$ G. Some of the field polarities are indicated by the black “+” and “-” signs.

The map demonstrates the complexity of the AR. The polarities at the sites of the EBs are seen better in Figs. 6 to 8. EB 1 was in a region of positive polarity within fields extending from the penumbra of the spot towards west. EB 2 was located between opposite polarity fields, where the stronger flux structure had the same polarity as the pores nearby and opposite to the polarity of the sunspot towards W (see Fig. 2). EB 3 was located close to an inversion line and showed two opposite polarity magnetic structures with polarity of the patch of stronger flux opposite to the polarities of the two spots towards E and W.

Figure 5 gives examples of observed $H\alpha$ profiles from EBs in comparison with the quiet Sun disc centre profile, for which we take the average from the flat fields. We note: (1) EBs affect little, if at all, the line minimum intensities, and the latter are in the same range as the average minimum intensity of the AR outside sunspots (see also Kneer 2010, Fig. 10); (2) the profiles of EBs may be very asymmetric; and (3) most important, the EB profiles are very bright in the wings at $\sim\pm 0.9$ Å off line centre, up to a factor of 2.5–3 brighter than the quiet Sun profile at these wavelength positions. These very bright EB profiles can also be seen in the work of Watanabe et al. (2011). Note that the $H\alpha$ profile has three H_2O blends at $\Delta\lambda = 0.71$ Å, 1.25 Å, and 1.40 Å.

4.2. Maps of Ellerman bombs and near surroundings

In Figs. 6 to 8 we show maps of intensities in broadband, in $H\alpha_{wing}$, for the minimum intensity of the IR line, for magnetic field strengths including polarities, for velocities from V zero-crossing, and for velocities from shifts of the minimum of the IR line. The alignment of the broadband and $H\alpha_{wing}$ images was

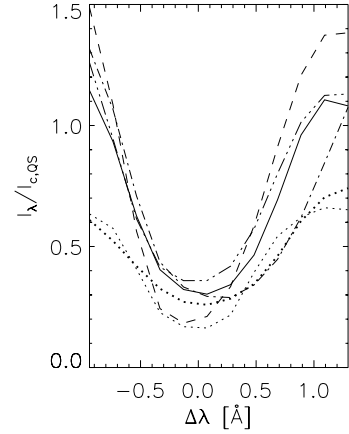


Fig. 5. Examples of observed $H\alpha$ profiles from Ellerman bombs (EBs) normalised to continuum intensity of quiet Sun profile; thin dotted: average profile of the flat fields from disc centre, normalised with profile from the FTS Atlas (Brautl and Neckel, quoted by Neckel 1999); thick dotted: average profile of AR near EB 2 outside sunspots and pores.

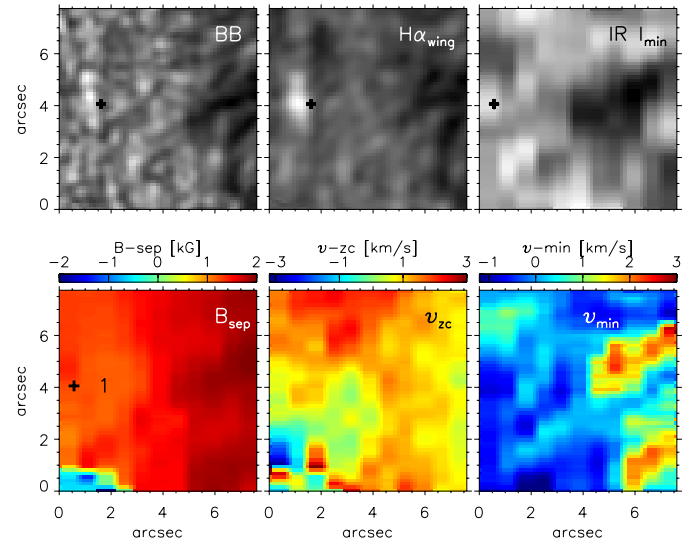


Fig. 6. Properties of EB 1 and surroundings. *Upper row from left to right:* intensities in broadband (BB), in $H\alpha_{wing}$ on logarithmic scale, and line minimum of IR $1.5648 \mu\text{m}$ line (IR I_{min}); *lower row from left to right:* magnetic field strength including polarity from separation of Stokes V lobes (B_{sep}), LOS velocity from Stokes V zero crossing (v_{zc}), LOS velocity from Doppler shift of minimum of IR line (v_{min}), positive velocities are away from observer. Terrestrial north is up, limb to the left; see text for black crosses.

performed by means of the sunspots and pores in the full FOV. For the alignment of the TIP vs. the TESOS images, the broadband images were convolved with a Gaussian with a width corresponding to $\sim 1''$. The alignment was then performed visually with an accuracy of ~ 0.2 .

The EBs studied here were associated with bright structures in the minimum intensity maps of the IR line. They are among the brightest structures and harbour magnetic fields of kG strength, but the IR continuum intensities are not conspicuous among the other faculae in the FOV without EB. The increase in minimum intensity can be caused by 1) heating deep down from magnetic field reconnection; 2) the Zeeman splitting; and 3) the increased temperature in magnetic flux tubes, which reduces absorption in Fe I lines within the tubes. The latter produces the

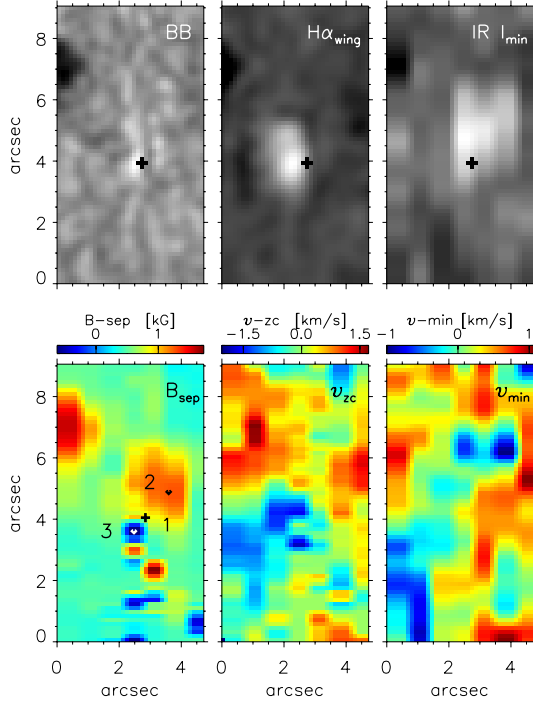


Fig. 7. Similar to Fig. 6 but for EB 2. Black and white bullets (marked with “2” and “3”) and cross: positions for which Stokes (Q, U, V) profiles were analysed (see Sect. 4.3.4).

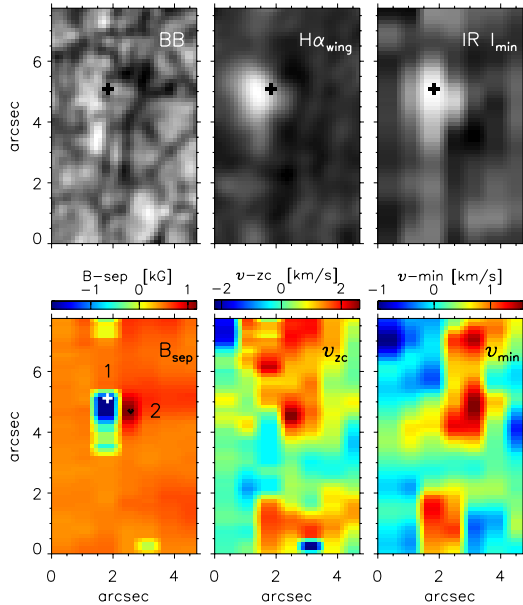


Fig. 8. Similar to Fig. 6 but for EB 3.

line gap phenomenon discussed by Sheeley (1967) and Kneer & von Uexküll (1991) among others.

The black crosses in the broadband images mark the positions of the maximum $H\alpha_{\text{wing}}$ intensities shifted towards W (right) by $0'.5$ to account for an adopted difference of formation height in broadband and $H\alpha_{\text{wing}}$ of ~ 500 km and a foreshortening by $\mu = \cos\theta = 0.69$ of the AR. This indicates the foot location of EBs, assuming that they stand straight up. The crosses also were transferred to the $H\alpha_{\text{wing}}$, IR line minimum, and magnetic field images. The $H\alpha_{\text{wing}}$ EBs appear to be located above granular structures of mean intensity. They are related

with bright granular faculae, which are also seen in IR line continuum, but not necessarily with the brightest broadband structures (see Figs. 1 to 3 above).

The magnetic field strengths in the maps B_{sep} and the velocities v_{zc} are to be taken with a grain of salt. We already mentioned the point and will come back to it below that the (Q, U, V) profiles often require multiple magnetic field structures. Yet the V profiles allowed a reliable determination of the lobe separation and zero crossing in patches with a strong field, $B \sim 1500$ G.

We now discuss briefly some features seen in Figs. 6 to 8 at the sites of the EBs and their surroundings. EB 1 had a field of mainly positive polarity, but we show in Sect. 4.3.4 that it also contains a negative polarity field. At the site of the EB at the height of the IR line formation, v_{zc} was $0 \dots 1$ km s $^{-1}$, while v_{min} was (0.0 ± 0.3) km s $^{-1}$. EB 2 had positive magnetic polarity, which is the same as the pore at the upper left border of Fig. 7. In its near surroundings the magnetic structure was complex with small patches of positive and negative polarity close to each other. At the site of the EB, v_{zc} and v_{min} were both in the range of -0.5 to $+0.5$ km s $^{-1}$. The dark patches close to the $H\alpha_{\text{wing}}$ EB stem from dark absorbing clouds that will be discussed below. EB 3 showed close opposite polarity fields next to each other with the $H\alpha_{\text{wing}}$ and IR I_{min} brightenings right between the two fields. This appears to have been a classical case of field reconnection in an Ω loop, or \cup loop. We show below that the magnetic fields in positions 1 and 2 underwent strong changes. The velocities in position 2 appeared to be large, v_{zc} and $v_{\text{min}} \geq 1$ km s $^{-1}$.

4.3. Temporal evolution of Ellerman bombs

4.3.1. Flows of granular pattern

Figure 9 shows the flow map of the entire TESOS broadband FOV around EB 2 located at the position of the black cross. It was determined from local correlation tracking during the time when EB 2 was observed. We do not see any prominent source or sink of the flow around the EB, as towards west or south of it, which could indicate emergence or submergence of magnetic field. There are flows towards the EB from north and away from it towards south-west, but only weak ones. Following a movie consisting of the broadband images along time, one also does not see any elongated granules near the site of the EB that would also indicate emergence of magnetic flux (Cheung et al. 2007).

4.3.2. $H\alpha_{\text{wing}}$ contrasts

The intensities of structures and of rms fluctuations are often given relative to some mean value or as contrasts. For spectral lines, the contrast profile $C(\lambda)$ is

$$C(\lambda) = \frac{I(\lambda) - I_0(\lambda)}{I_0(\lambda)}, \quad (6)$$

where $I(\lambda)$ is the intensity measured from the structure under study and $I_0(\lambda)$ is the reference intensity, which is usually an average profile from a nearby non-disturbed area.

Figure 10 shows the temporal evolution of the contrasts in $H\alpha_{\text{wing}}$ and in the broadband of the three EBs under study. The $H\alpha_{\text{wing}}$ intensities fluctuate on timescales of a few min, as was noted by Qiu et al. (2000), Pariat et al. (2007), and Matsumoto et al. (2008).

It was noted above that EBs are closely related to a broadband facula. The position of the maximum broadband contrast was often close to that of the EB in $H\alpha$. This is reflected in the

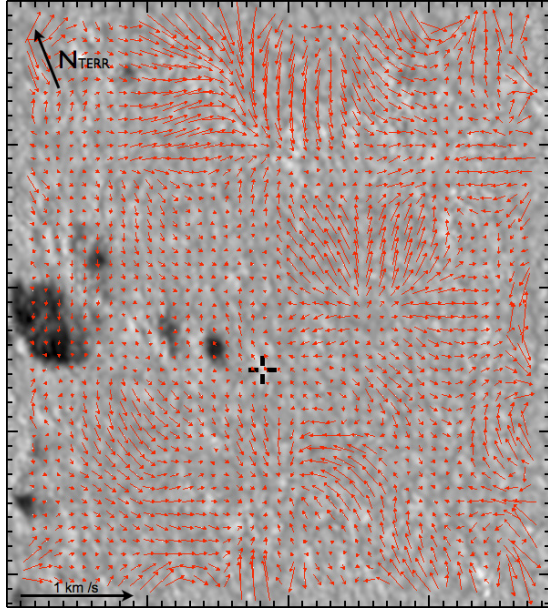


Fig. 9. Flow map of the area surrounding EB 2 from local correlation tracking. Scale of velocity at bottom, tickmarks in arcsec, black cross: position of EB, arrow at upper left corner: direction of terrestrial north, i.e. same orientation as in Figs. 1 to 3.

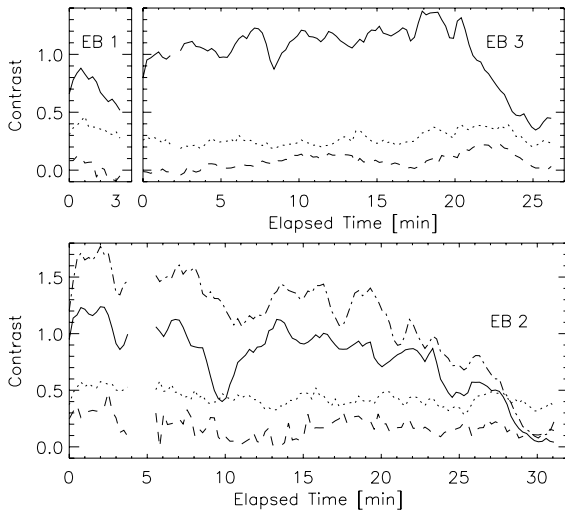


Fig. 10. Temporal evolution of contrasts C of the three EBs under study; solid: maximum C of EBs from $H\alpha_{\text{wing}}$, dash-dotted for EB 2: maximum C from blue wing alone; dashed: C of broadband image (at 6300 \AA) at position of maximum of $H\alpha$ EB, shifted by 0.5 ; dotted: maximum C of broadband in the facula associated with the EB. Elapsed time is time since start of observation of the particular target.

high contrast of the faculae in broadband, but also often another facular point was brighter.

The facula related to EB 2 developed into a chain of facular points, which dissolved when time went on. When the $H\alpha_{\text{wing}}$ brightness had died out, the broadband facula continued to have high contrast. Yet again, the broadband facular points related to the EB are not necessarily the brightest in the AR. The $H\alpha$ intensity of this EB strongly decreased ~ 10 min after the start of its observation and then recovered. The blue side of $H\alpha$ decreased less. Inspection of the $H\alpha$ profiles showed that this intensity decrease is due to dark, absorbing clouds crossing the EB from W

to E (see also Figs. 7 and 11). The EB profiles during minimum intensity look similar as the dash-dotted profile in Fig. 5. We suggest that at least part of the brightness fluctuations of EBs, as seen in Fig. 10 and also reported by Qiu et al. (2000) and Pariat et al. (2004), are due to varying absorption by dark clouds.

EB 3 was, at some times during its life, the brightest among the studied EBs. The $H\alpha_{\text{wing}}$ contrast reached 1.4, that is it was almost a factor of 2.5 brighter than the average reference intensity. Yet it was only rarely related to a facular point or chain. Most of the time, the $H\alpha$ brightness occurred above abnormal granulation seen in broadband. The broadband contrasts at the EB position (shifted by 0.5) and the highest broadband contrast near the EB are not exceptional with values of ~ 0.1 – 0.3 .

4.3.3. Evolution of intensities and magnetic fields

Figure 11 shows the temporal evolution of maps from EB 2 in broadband, $H\alpha_{\text{wing}}$, IR I_{min} , and B_{sep} . The black crosses are placed the same way as those in Figs. 6 to 8. They move towards the upper or lower boundary, depending on the position of the highest $H\alpha_{\text{wing}}$ intensity within the EB. The sequence starts after the interruption of observation of this EB and continues until we stopped, when the $H\alpha_{\text{wing}}$ brightness had definitely faded. The four series of images are scaled each to their minima and maxima within the sequence. The black crosses again indicate the positions of maximum $H\alpha_{\text{wing}}$ contrast shifted west by 0.5 . We point out several properties of the evolution:

1. The broadband facula is related with the $H\alpha_{\text{wing}}$ brightness, but its temporal evolution appears to be independent.
2. The dark, absorbing clouds that crossed the $H\alpha_{\text{wing}}$ EB are visible during the whole sequence, especially well around the fourth image and in the last five images of Fig. 11.
3. The IR line minimum intensity and the magnetic field maxima appear to be shifted towards north by ~ 0.5 compared to the $H\alpha_{\text{wing}}$ EB.
4. The EB occurred at the boundary of the patch with strong magnetic field; at $\sim 1''$ towards south-west of the EB, weak-flux features with opposite polarity are visible from time to time. Towards the end of the lifetime of the EB, its position had drifted into the centre of the strong-field structure and of the IR line minimum facula.
5. The relative IR line minimum intensity I_{min}/I_c does not appear to depend on the $H\alpha_{\text{wing}}$ brightness. Its maximum varies uncorrelated with the $H\alpha_{\text{wing}}$ contrast by 0.035. It is still visible without noticeable decrease at the end of the sequence when the $H\alpha$ EB had faded. It is thus just a normal line gap.
6. The magnetic field at the IR line minimum facula stays high, even beyond the fading of the EB. It is surrounded by a complex assembly of small patches of fields with both positive and negative polarity. Their extension in north-south direction is often smaller than the spatial resolution of the TIP data, which we estimate from the slit width and scanning step width to be $1''$ – $1.5''$. The magnetic patches change in time. Yet, it is not clear whether these changes are intrinsic, that is solar, or due to variable resolution.

These findings do not allow any straight forward conclusion about the cause of this EB 2. Possibly it is the messy magnetic structure surrounding it that leads to field reconnection, but it remains unclear why the EB died out, although the field structure within it and surrounding it has retained its strength and complexity. It is also possible that this EB was caused by reconnection of the strong field in the EB with fields outside the FOV, or high in the atmosphere, with different rooting.

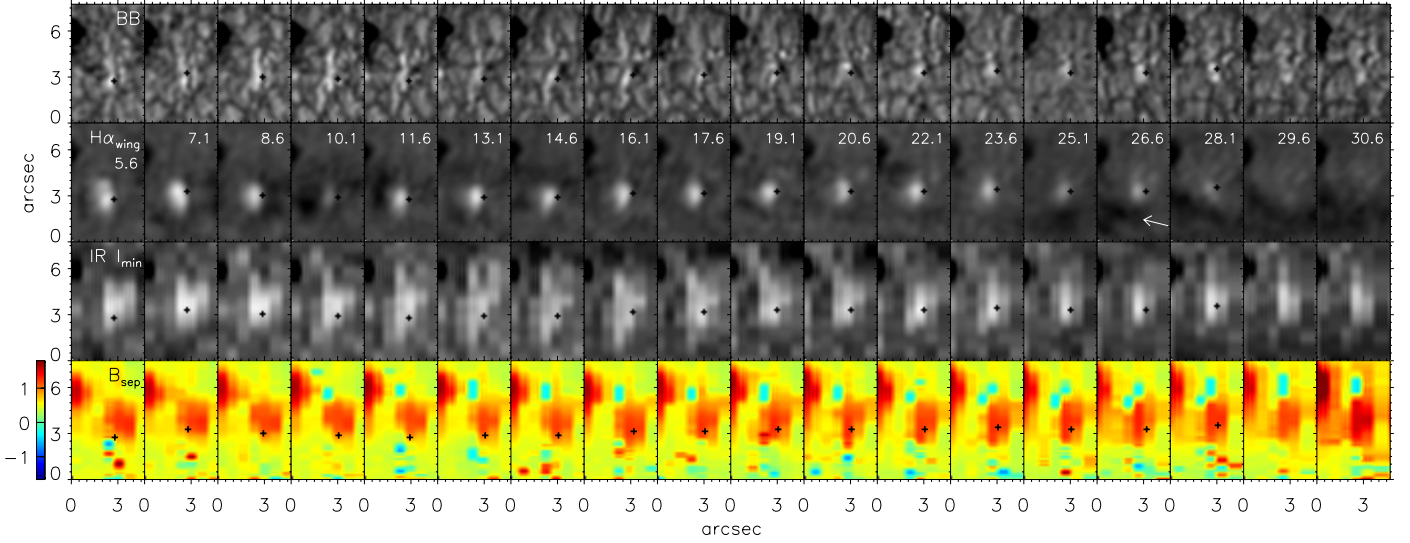


Fig. 11. Temporal evolution of EB 2 after interruption of its observation (see Fig. 10). Maps with cadence of 90 s from *left to right*. *Top row*: broadband (BB); *second row*: $H\alpha_{\text{wing}}$ with times (in min) since start of observation of this EB; *third row*: minimum intensity of IR line; *fourth row*: B_{sep} from separation of Stokes V amplitudes including sign; black crosses as in Figs. 6 to 8. Numbers at the colour bar are field strength in kG. Arrow in last fourth $H\alpha_{\text{wing}}$ image indicates absorbing, dark clouds crossing from W to E in lower part of map.

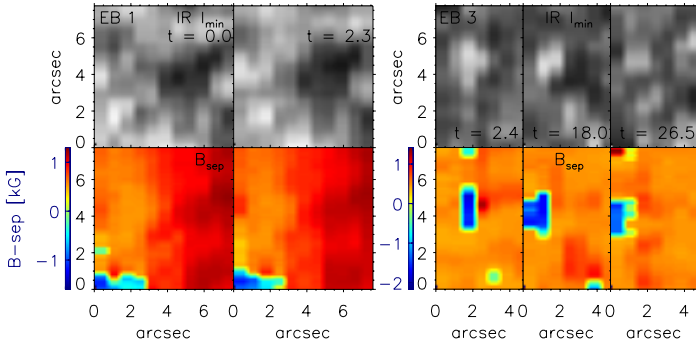


Fig. 12. IR line minimum intensities and magnetic fields from separation of Stokes V lobes from EB 1 (*left*) and EB 3 (*right*) at selected times since start of observation of specific EB. t is in min; numbers at colour bars are in kG.

IR line minimum intensities and magnetic fields of EB 1 and EB 3 from some temporal positions are given in Fig. 12. EB 1 was observed only a short time until its $H\alpha_{\text{wing}}$ contrast had declined. We cannot see any clear signature of changes in the magnetic field structure of this EB as the reason for the fading of the $H\alpha$ EB. Small variations of the fields with negative polarity near the lower border of the FOV are obvious, but these were some $3''$ away from the site of the EB, as seen in Fig. 6.

Unlike EB 1 and EB 2, large changes in the IR I_{min} and B_{sep} maps from EB 3 (right part of Fig. 12) were detected. We suggest that this EB represents a case of field reconnection near the formation of $H\alpha_{\text{wing}}$ brightness, close in height and horizontal position. The relative IR I_{min}/I_c intensity at the position of the EB had decreased at the end of the observing sequence at $t = 26.5$ min by 0.05. This is a substantial amount considering that this 1.5648μ line is weak. Right at the position of this EB, magnetic fields of opposite polarity are located. The positive polarity becomes weaker along the time sequence, as seen from the temporal position at 18 min, when the $H\alpha_{\text{wing}}$ contrast was maximum. The negative polarity field drifted towards east and dispersed, while the positive polarity field diminished. We shall

come back to this behaviour when discussing the evolution of (Q, U, V) profiles.

The three EBs studied here are also seen in SDO-AIA images at 1600 \AA and 1700 \AA . The AIA 1600 \AA filter transmits the strong CIV emission lines at 1550 \AA formed at temperatures of 10^5 K (see Lemen et al. 2012, Table 1). The 1700 \AA spectral region is thought to be formed at high photospheric layers (of the quiet Sun). We noticed many transient small-scale ($\sim 1''$) brightenings of various lifetimes and amplitudes in the AIA movies of the AR, which were not so conspicuous in $H\alpha_{\text{wing}}$. We counted the brilliant transients in the 1600 \AA channel and detected ~ 300 events between 07:30 UT and 09:30 UT in a $162'' \times 144''$ area of the AR. A detailed analysis of the brightenings in the AIA 1600 \AA and 1700 \AA channels and a determination of the contributing atmospheric heights are beyond the scope of the present work.

Figure 13 depicts time sequences of the maximum intensities of EB 1 to EB 3 as seen in the AIA data. EB 1 is the least conspicuous. Its brightening lasted for ~ 10 min in 1600 \AA , but it continued with brightness eruptions of a few min duration in 1700 \AA after we had stopped its observation with TESOS and TIP. The AIA 1700 movie shows also a persistent twinkling along a line parallel to the border of the penumbra seen in Fig. 1.

For EB 2, the brightness variations were similar in 1600 \AA and 1700 \AA , the flaring lasted for ~ 50 min. The intensity dip around 08:22 UT coincides in time with that seen in $H\alpha_{\text{wing}}$ (cf. Fig 10). We had there found that it was due to absorbing high clouds, which are not conspicuous in the AIA movies.

EB 3 started at $\sim 08:35$ UT in the AIA data. It had faded at $\sim 09:12$ UT after a slow decline in 1700 \AA and at $\sim 09:12$ UT after a rapid intensity decrease in 1600 \AA .

4.3.4. Evolution of IR Stokes (Q, U, V) profiles

Figures 14 to 18 show $(Q_\lambda, U_\lambda, V_\lambda)$ profiles from the three EBs under study and from their surroundings, as measured with TIP (dotted), fitted with Gaussians (dashed), and suggested above in Sect. 3.2. All profiles are normalised to the local continuum

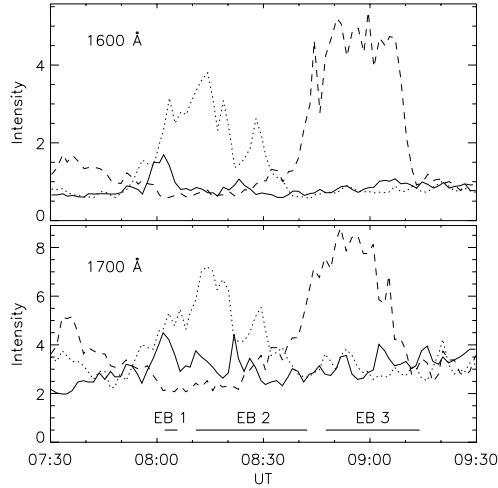


Fig. 13. Temporal evolution of maximum intensities (in arbitrary units) observed by AIA. Solid: EB 1, dotted: EB 2, dashed: EB 3; time step 90 s; horizontal bars: times of observation of EB 1 to EB 3 with TESOS and TIP.

intensity of the I_λ profiles. It is obvious that V profiles like the ones in Fig. 14 cannot be represented by two Gaussians, which lead to fits far from four lobes. These profiles require two magnetic field structures within the resolution element (see also Rüedi et al. 1992; Solanki et al. 1992). We note that four-lobed V profiles were also seen away from any EB but close to magnetic inversion lines. The resolution of our IR observations was too low to see a spatial separation of fields with opposite polarity.

To get better insight into the field structures, we fitted some of the measured profiles with two magnetic structures embedded in a non-magnetic surrounding by trial and error. For each structure, we adopted the Milne-Eddington approximation and used the analytic solution given by Landi Degl’Innocenti (1992). All three atmospheres were represented by the same run of the source function S with continuum optical depth τ along the LOS

$$S(\tau) = S_0 + S_1\tau. \quad (7)$$

We chose $S_0 = 1$ and $S_1 = 0.75$, which mimics the intensity ratio at 1.565μ for surface temperature $T(\tau = 0) = 4600$ K and $T(\tau = 1) = 6000$ K in LTE. The ratio of line to continuum opacity was chosen to $\eta_0 = 0.2$, which with the choice of S_0 and S_1 , gave approximately the correct line depression of the average intensity profile I_λ . Magneto-optical effects were not considered, they are negligible for the transfer of the weak IR lines. The I_λ profiles were also not fitted, nor did we consider a crossing of rays through various magnetic structures. We performed one-dimensional transfer calculations.

The free parameters to represent the measured $(Q_\lambda, U_\lambda, V_\lambda)$ profiles are then for each of the magnetic structures: field strength B , inclination vs. LOS γ , azimuth χ , velocity along LOS v , Doppler width $\Delta\lambda_D$, and filling factor f of the structure within the resolution element.

The results of the fitting are depicted for some positions in space and time by the solid profiles in Figs. 14 to 18. The agreements are not perfect, strong asymmetries are difficult to simulate, especially when Q , U , and also sometimes the V profiles require different flows. However, the fits give much more reasonable physical parameters than the fitting by just three Gaussians for (Q, U) and two Gaussians for V . The (Q, U) profiles that often have narrow central π components and broad σ components

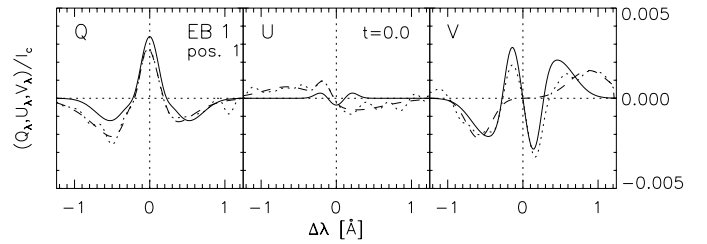


Fig. 14. Stokes (Q, U, V) profiles from EB 1 at position 1 in Fig. 6 at the beginning of the observation of this EB; dotted: measured profiles after filtering, dashed: fitted with Gaussians as described in Sect. 3.2, solid: fitted with Milne-Eddington approximation, assuming two magnetic structures embedded in a non-magnetic atmosphere. t is time in min since start of observation of EB 1.

and the V profiles that have four lobes are adequately reproduced, considering the simple models.

The parameters of a few magnetic structures from the fitting are collected in Table 1. From varying the parameters we found that the fitting within the Milne-Eddington approximation is sensitive to the magnetic field strength within ± 50 G for fields ≤ 600 G and within ± 100 G for fields ≥ 1400 G. The inclinations γ and azimuths are accurate to $\pm 10^\circ$ away from the changes of sign but are more accurate, to $\sim \pm 5^\circ$ near 90° for the inclination and near 45° and 135° for the azimuth. The velocities v could be determined to $\sim \pm 0.2$ km s $^{-1}$ for low velocities and to $\sim \pm 0.4$ km s $^{-1}$ for velocities ≥ 2 km s $^{-1}$. We estimate the accuracy of the Doppler widths to $\sim \pm 0.02$ Å. Finally, the accuracy of the filling factors f is $\sim \pm 0.01$ for $f \leq 0.1$ and $\sim \pm 0.03$ for $f > 0.1$. We now discuss the results of the fittings to the measurements, shown as (Q, U, V) profiles in Figs. 14 to 18 and in Table 1.

Ellerman bomb 1. We consider the measured (Q, U, V) profiles adequately represented by the two-fields fitting. A problem often arises with the need for velocities for either Q , U , or V which destroy the good fits to the other profiles. Generally, asymmetries are difficult to achieve with the simplified method, that is with Milne-Eddington approximation and with radiative transfer in plane-parallel atmospheres.

Two fields with filling of ~ 0.1 are needed to explain four-lobed V profiles. One component had ~ 1000 G and showed negative polarity, $\gamma \approx 120^\circ$ with respect to LOS, i.e. the same polarity as the two spots towards west of this EB as seen in Fig. 4. The weaker, positive-polarity field with ~ 300 G had a $\gamma \approx 50^\circ$, it could have had a vertical or a horizontal orientation with respect to the solar surface. The azimuths of the fields were $\sim 90^\circ$. We remind the reader that the heliocentric angle of the observations was 46° on average, while the direction to the limb corresponded to $\chi \approx 90^\circ$.

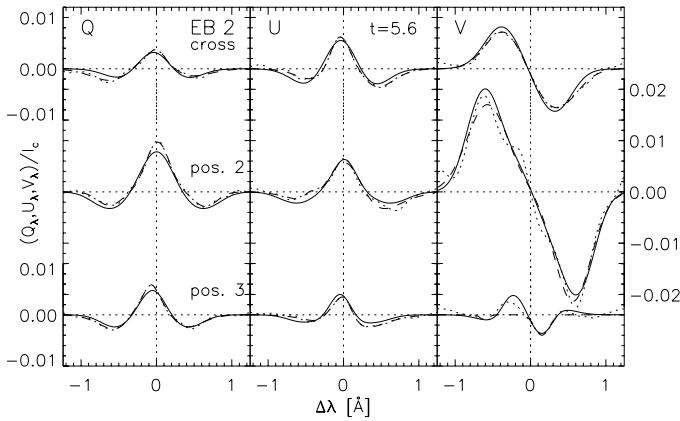
We had seen, that there were repeated brightenings along a line towards terrestrial north and parallel to the penumbra west of EB 1 (see Figs. 1 and 4) in the AIA data. Possibly, this line of flaring events reflected magnetic flux bundles emerging near the evolving sunspot and recombination in a “sea serpent” topology in continuation of the penumbral magnetic fields. Higher spatial resolution, larger fields of view, and longer observational time spans in similar situations should help reveal the correct picture.

Ellerman bomb 2. Figure 15 depicts the (Q, U, V) profiles from positions 1–3 in Fig. 7 at time $t = 5.6$ min. The profiles can be

Table 1. Examples of magnetic field parameters in and near Ellerman bombs (EBs) 1 to 3 at positions marked in Figs. 6 to 8.

Position	t [min]	B_1, B_2 [G]	γ_1, γ_2 [°]	χ_1, χ_2 [°]	ν_1, ν_2 [km s ⁻¹]	$\Delta\lambda_{D,1}, \Delta\lambda_{D,2}$ [Å]	f_1, f_2
EB1, cross	0.0	300, 1200	50, 120	80, 90	0.0, 0.0	0.15, 0.33	0.075, 0.075
cross	2.3	300, 1000	50, 115	100, 75	0.0, 0.0	0.15, 0.33	0.1, 0.1
EB2, pos.2	5.6	500, 1750	45, 35	130, 107	0.4, 0.0	0.18, 0.33	0.055, 0.4
pos.3	5.6	500, 1200	125, 105	65, 75	-0.8, -1.2	0.18, 0.30	0.075, 0.105
cross	5.6	900, 1000	45, 65	120, 120	-0.4, -1.0	0.28, 0.28	0.1, 0.175
cross	11.6	800, 1000	60, 85	120, 90	0.0, -1.0	0.28, 0.40	0.25, 0.24
cross	22.1	700, 1800	25, 50	120, 115	-1.9, 1.0	0.20, 0.20	0.15, 0.15
max. B	29.6	500, 1750	45, 35	130, 107	0.4, 0.0	0.18, 0.33	0.055, 0.4
EB3, cross	2.4	400, 1650	70, 120	105, 85	0.3, 0.0	0.18, 0.20	0.175, 0.225
cross	26.5	550, 1650	55, 110	95, 87	1.0, -0.4	0.18, 0.20	0.065, 0.08
pos.2	2.4	450, 1450	25, 35	105, 100	0.4, 1.5	0.17, 0.25	0.275, 0.05
pos.2	26.5	450, 1550	50, 35	80, 120	0.5, 0.0	0.17, 0.25	0.23, 0.11

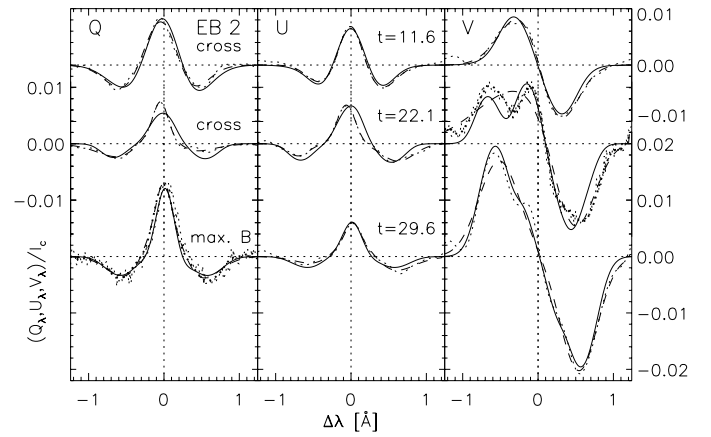
Notes. Time t of start of scan since beginning of observation of specific EB, field strengths B , inclinations vs. LOS γ , azimuths χ (counterclockwise from terrestrial north), LOS velocities ν (positive away from observer), Doppler widths $\Delta\lambda_D$, and filling factors f .


Fig. 15. (Q, U, V) profiles from EB 2, positions 1 (=cross) to 3 in Fig. 7. Same time is used as in first column of maps in Fig. 11.

well represented by three Gaussians for (Q, U) , respectively, by two Gaussians for V , except for the weak V profile at position 3. For the site of the EB, the two-field fitting (Table 1) gives field strengths of ~ 1000 G, an inclination of 45° – 65° , and an azimuth of 120° . From the position of the AR on the solar disc ($\theta \approx 45^\circ$, terrestrial north up in Fig. 7), one may conjecture that the field at the position of the cross was inclined towards position 3 in Fig. 7, which contained some field with opposite polarity. At the maximum-field position 2, we found strong fields of ~ 1750 G with an inclination slightly away from the pore (see Fig. 7) but close to the vertical and a large filling of 0.4.

The (Q, U, V) profiles at the site of this EB at other times are depicted in Fig. 16. Figure 11 shows that the configuration at $t = 11.6$ min appears similar to that at 5.6 min, the field strength is also ~ 1000 G with larger filling. Yet the inclination has increased leading to larger (Q, U) profiles relative to V . At $t = 22.1$ min, the site of the EB was on the way towards the centre of the strong field patch. The corresponding V profile requires two magnetic field components, one of 700 G and a strong field component with 1800 G.

Finally the magnetic field structure at the position of maximum field, when the EB had faded at $t = 29.6$ min, is very similar to the one at 5.6 min at the same position. The (Q, U, V) profiles can be represented by the same field configuration.


Fig. 16. Temporal evolution of (Q, U, V) profiles from EB 2; positions: crosses in 5th and 12th columns in Fig. 11 at $t = 11.6$ min and 22.1 min, respectively, and maximum of B in 2nd last column of same figure for $t = 29.6$ min; thin and thick dotted V profiles at $t = 22.1$ min. Q profiles at $t = 29.6$ min are unfiltered and filtered profiles, respectively.

Tentatively, we interpret the evolution of this EB and of the observed field configuration as reconnection at the side of the strong field patch with weaker opposite polarity fields rooted next to it. The flaring ceased when the reconnection site had moved up in height and the magnetic structure had relaxed.

Ellerman bomb 3. When extracting the (Q, U, V) profiles for this EB, we followed the drifts seen in the right part of Fig. 12. As already noted in the discussion of this figure, we observed strongest changes in this EB. At position 1, the strong field of 1650 G remained large, but its filling factor decreased from 0.225 to 0.08 at the end, when the EB faded. The inclination of this component was such to give the correct sign of V , or negative polarity, and a large Q signal, while the azimuth was close to 90° . The weak-field component had positive polarity and contributed to the four-lobed V profile.

At position 2, both field components had small inclinations at the beginning of the sequence, producing strong V profiles. During the maximum brightness of this EB at $t = 18$ min, the filling factor of the strong field component increased greatly, while its inclination had turned almost to a direction

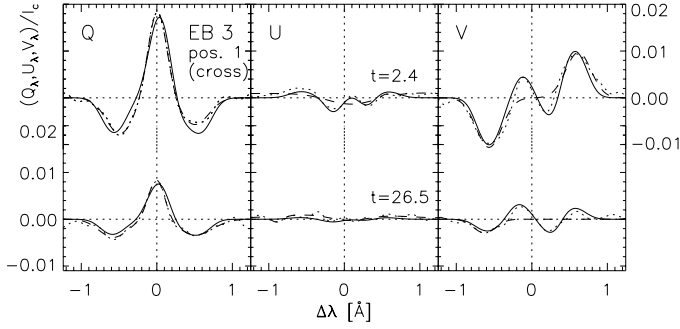


Fig. 17. Similar to Fig. 14 but for EB 3 and position 1 in Fig. 8.

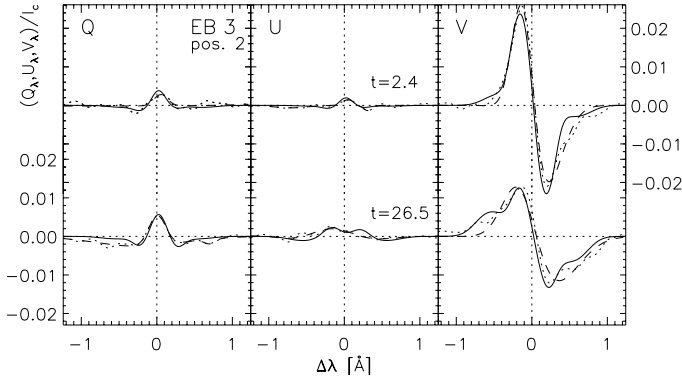


Fig. 18. Similar to Fig. 17 but for position 2.

perpendicular to LOS, producing a broad Q profile and broad wings in the V profile. At the end, the strong-field component had returned its inclination to closer to LOS, and its filling factor had weakened. The azimuths were near 90° , the U profiles were small. Again, we conclude from the strong changes of the fields of this EB that it was likely produced by magnetic field reconnection in the vicinity in both atmospheric height and perpendicular to it.

With some efforts, the fitting by trial and error can be improved by applying inversions of all four Stokes profiles and also of the weaker FeI 1.5653μ line, assuming again the Milne-Eddington approximation. All the parameters, including the thermal structure of the magnetic and non-magnetic atmospheres, were then to be free parameters. In an automated way, the magnetic structures in the whole FOV of all scans with TIP can be determined. A more sophisticated treatment of the radiative transfer with rays crossing several magnetic and the non-magnetic structures and with velocity gradients or even velocity jumps at the interfaces (Sánchez Almeida et al. 1988; Grossmann-Doerth et al. 1988) would also yield better agreement between measured and fitted (Q , U , V) profiles. Yet we consider the approach chosen for the present study already instructive in the search of magnetic fields, especially of their temporal variation, which could cause EBs by field reconnection.

Finally, inspection of Table 1 reveals the general trend that large magnetic fields from the fitting require larger Doppler widths than weaker fields. We speculate that this is caused by a distribution of magnetic field strengths within each magnetic component. Without any microturbulence, the Doppler width for the 1.5648μ line at 6000 K is 0.07 \AA , the Doppler widths in Table 1 are always larger, most times much larger. The filtering of the profiles has no influence on the widths, as seen from Fig. 16.

4.4. Atmospheric structure from two-dimensional $H\alpha$ modelling

We studied which small-scale structures embedded in an atmospheric plage model are compatible with the EBs observed in $H\alpha$ by means of two-dimensional (2D) non-LTE radiative transfer. The method and the results are described below.

4.4.1. Modelling procedure

We performed calculations of $H\alpha$ profiles from structures embedded in a static, undisturbed atmosphere. For simplicity and fast modelling, the non-LTE radiative transfer for $H\alpha$ was performed in the approximation of a two-level plus continuum atom. For this atomic model, the line source function S_l is (see Mihalas 1970)

$$S_l = \frac{\int J_\lambda \phi(\lambda) d\lambda + \varepsilon B + \eta B^*}{1 + \varepsilon + \eta}, \quad (8)$$

where J_λ is the angle averaged intensity, $\phi(\lambda)$ is the normalised absorption profile, B is the Planck function, ε is the ratio of collisional to radiative de-excitation from hydrogen level 3 to level 2, and η and B^* contain the radiative and collisional routes to and from the continuum level of hydrogen to the second and third level. Continuous background absorption and emission in LTE are added to get the wavelength-dependent source function

$$S_\lambda = \kappa_\lambda S_l / (\kappa_\lambda + \kappa_c) + \kappa_c B / (\kappa_\lambda + \kappa_c), \quad (9)$$

where κ_λ and κ_c stand for the line absorption and continuous absorption coefficient, respectively.

For the undisturbed background atmospheric model, we used the static plage model FALP of Fontenla et al. (1993) with a small modification: its run of temperature was reduced in the chromosphere and transition region linearly by $\Delta T = 0 \text{ K}$ at 1000 km to $\Delta T = -530 \text{ K}$ at 1730 km. The hydrogen departure coefficients were kept as in the original model. The modification ensures that no line emission occurs from the undisturbed model with this simple treatment of the hydrogen atom. The radiation temperatures for the Balmer and Paschen continua were chosen as 5800 K and 5600 K, respectively. Partial redistribution for the $H\alpha$ line formation was applied for tests, yet it turned out to be not important. Figure 19 depicts the $H\alpha$ profiles from this model at disc centre and at $\cos \theta = 0.69$ in comparison to the profile from the FTS atlas, which is also from disc centre. The intensities around line minimum of the calculated profiles are not very accurate, because they are formed partly in the transition region where the steps in optical depth are coarse.

The parameters $P_0(z) = \{\varepsilon_0, \eta_0, B_0, B_0^*, \kappa_{\lambda,0}, \kappa_{c,0}\}$ with index “0”, indicating standard values, are calculated from the modified FALP atmospheric model. Into the background model, periodic 2D structures were embedded along the lines as described in Al et al. (2004, Sect. 3.3 there). Periodic structures were chosen, because the conditions then at the side boundaries are formulated to the same accuracy as inside the structures. We chose fluctuations, which were not necessarily small, of any of the parameters P , according to

$$P(x, z) = P_0(z) \cdot \left(1 + \sum_i \Delta_i(x, z) \right), \quad (10)$$

where the Δ_i are of the form

$$\Delta_i(x, z) = \Delta_{0,i} \cdot \exp \left\{ - \left[(z - z_i) / \Delta_{z,i} \right]^2 \right\} \cdot \exp \left\{ - \left[(x - x_i) / \Delta_{x,i} \right]^2 \right\}. \quad (11)$$

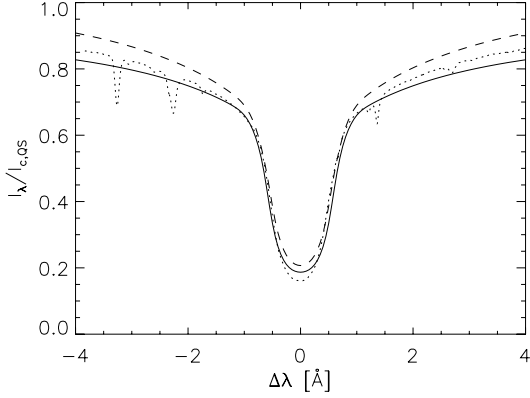


Fig. 19. $H\alpha$ profiles; dotted: from FTS Atlas; dashed: calculated from modified Fontenla et al. (1993) plage model FAL P at disc centre; solid: from same model at $\mu = \cos \theta = 0.69$. Calculated profiles are normalised to disc centre continuum intensity at $\lambda 6563 \text{ \AA}$ given in Harvard Smithsonian Reference Atmosphere (HSRA, Gingerich et al. 1971).

The summation over i in Eq. (10) thus goes over all structures at specific positions (z_i, x_i) and with widths ($\Delta z_i, \Delta x_i$). The x direction is assumed perpendicular to the solar limb. The z direction is normal to the solar surface. We chose a period along the horizontal x -coordinate of 1800 km with spacing of 60 km. With sufficiently small structures in x , the choice of the long period of 1800 km leads to only little, if any, influence via radiative transfer from one period to the other. The vertical z -coordinate ranged from -109 km (sub-photosphere) to 1734 km (base of the transition region), and the steps were between 7 km to 35 km. Figure 20 gives two examples of parameter variations on the atmospheric background model.

The parameters η and B^* will not be subjected to variations. Test modelling has shown that they are unimportant. In the FAL P model, $\eta \cdot B^* > \varepsilon \cdot B$ only around the temperature minimum which is transparent to $H\alpha$ photons (see Kneer 2010), and B^* is fixed by the radiation in the Balmer and Paschen continua from the deep photosphere. The EBs are considered to occur in a height range from low photosphere to low chromosphere. High EB intensities require local temperature increases or of Planck function B , variations in opacity κ_λ and κ_c , and variations in ε .

The source function $S(x, y, \lambda)$ was calculated iteratively with the 2D non-LTE code developed by Auer et al. (1994), which uses Ng's (1974) acceleration technique. Once the iterations were converged, we calculated the emergent $H\alpha$ profiles across the periodic structure along the x -coordinate, solving the radiative transfer equation for rays under the angle $\theta = 46^\circ$.

The line absorption $\kappa_\lambda(x, z)$ contains several parameters that can change across x (and z): 1) the number density n_2 of absorbing hydrogen atoms in level 2 (and in level 3, but stimulated emission is negligible); 2) the Doppler width $\Delta\lambda_D$; 3) the damping parameter Γ ; and 4) the Doppler shift due to a macroscopic velocity. The first three parameters were included in the calculation of the source function. A Doppler shift increases substantially the complexity of the 2D code. Velocities were therefore applied only in the formal solution. One-dimensional test calculations had shown that the changes of the source function due to macroscopic, height dependent velocities do not alter the contrast profiles beyond the accuracy of the measurements. The conclusions from our modelling will remain the same. Like η and B^* , the damping parameter Γ will not be varied either in the 2D modelling. Its change during an EB is difficult to assess. The $H\alpha$ damping wings are caused by radiative damping and partly

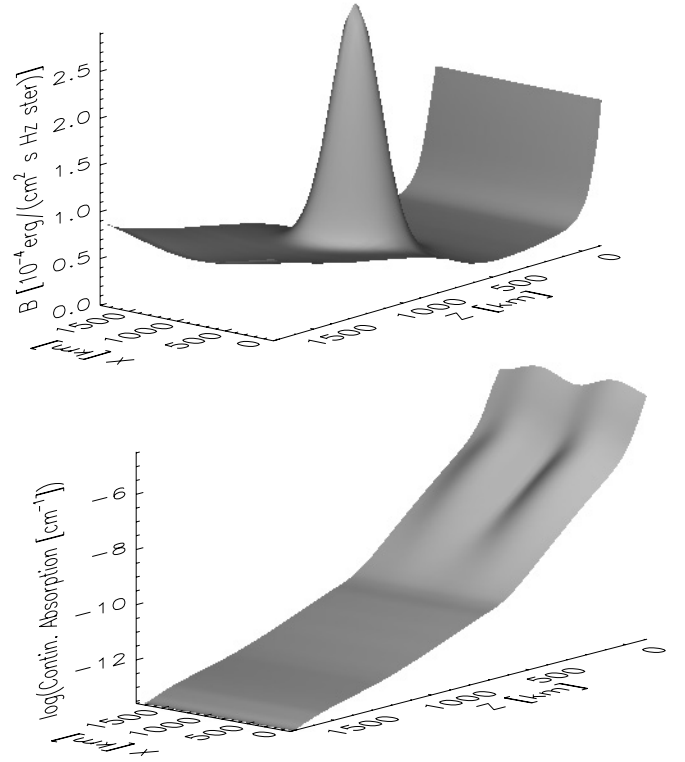


Fig. 20. Two examples of parameter variations in x and z on (modified) background model FAL P (Fontenla et al. 1993) without highest layer in transition region; upper panel: Planck function $B(x, z)$, lower panel: $\kappa_c(x, z)$ on logarithmic scale.

by collisions with neutral hydrogen atoms with the latter only being important in deep photospheric layers with sufficient neutral hydrogen. Georgoulis et al. (2002) had estimated a hydrogen ionisation degree of $\chi \approx 0.89$ at the location of the EB.

4.4.2. Contrasts from models

We now study the influence of the height where the EB may occur and the influence of the amplitudes of the various parameters. We place Planck function increases at $z_i = 300 \text{ km}$ into the photosphere of the background model, at $z_i = 500 \text{ km}$, which is around the temperature minimum, and at $z_i = 800 \text{ km}$, which is in the low chromosphere. The modelling had shown that at larger heights, above 1000 km , the $H\alpha$ profiles get strong emissions around $\pm 0.65 \text{ \AA}$ off line centre and no contrasts out in the wings beyond 1 \AA , which are much different from the observed EB profiles. We chose for the extension in height always $\Delta z = 150 \text{ km}$ (cf. Eq. (11)), giving a FWHM of $\sim 250 \text{ km}$, and for the horizontal extension $\Delta x = 250 \text{ km}$, or a FWHM of $\sim 415 \text{ km}$.

Figure 21 gives some examples of contrasts of the $H\alpha_{\text{wing}}$ intensities and the continuum intensities (at $+20 \text{ \AA}$ off line centre) across the periodic structure. The abscissa in Fig. 21 is foreshortened for oblique viewing. We started the (oblique) ray calculation at the upper right corner, that is to the right and at the top of the periodic structure. The absolute position of the contrasts along the abscissa are not relevant, and the contrasts in Fig. 21d were shifted in x by one-half period for clarity. The rays from the bottom of the model have actually already traversed more than one period in x before reaching the upper right corner. Yet, the relative positions of the continuum and $H\alpha_{\text{wing}}$ contrasts are important, they are formed at different heights.

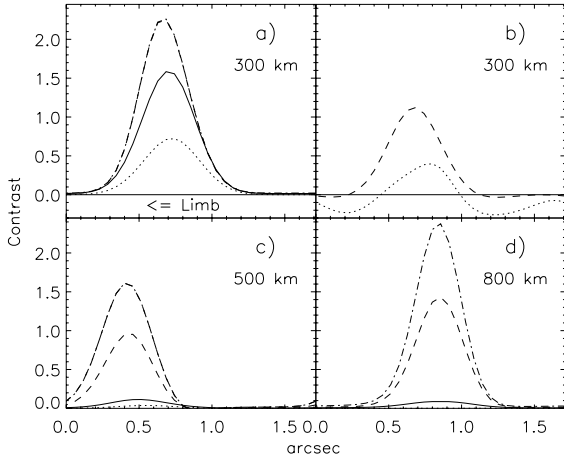


Fig. 21. Examples of modelled contrasts with various parameters. Heights of centres of modifications of atmosphere are given in the figure. Abscissa in arcsec covers one period in x , it is foreshortened for oblique viewing. Solid horizontal lines: zero contrast level; dotted: continuum contrast (at $+20 \text{ \AA}$ from line minimum); solid: $H\alpha_{\text{wing}}$ contrast with increased Planck function ΔB ; dashed: solid plus increased line opacity $\Delta\kappa_{\lambda}$, dash-dotted: dashed plus increased coupling to Planck function $\Delta\varepsilon$. See text for values of parameters.

Except for Fig. 21b, the amplitude of the increase in the Planck function was chosen to $\Delta_{0,B} = 7$ (see Eq. (11)), which translates into temperature increases by factors of 1.85 at $z_i = 300 \text{ km}$, 1.82 at $z_i = 500 \text{ km}$, and 2.1 at $z_i = 800 \text{ km}$. These values are larger than the temperature increase by a factor of ~ 1.3 at the reconnection site estimated by Kitai (1983) from observations and by Archontis & Hood (2009) from numerical simulations.

The dotted curves in Fig. 21 are the calculated contrasts of the continuum. The solid curves in this figure result from just an increased Planck function. Fig. 21a was calculated with the $\Delta_{0,B}$ given above (solid) and with the same $\Delta_{0,B}$ plus an increase in the amplitude of line opacity $\Delta_{0,\kappa_{\lambda}} = 5$ (dashed) which accounts for an increase in hydrogen atoms in level 2 from a density increase and higher excitation. A substantial increase in ε by an amplitude $\Delta_{0,\varepsilon} = 150$ has no influence (dash-dotted). At a height of 300 km, the $H\alpha$ wing is formed in LTE.

Temperature increases at low photospheric heights ($z_i \approx 300 \text{ km}$) appear to produce inevitably increased continuum contrasts (see dotted contrast curve in Fig. 21a). This is not always observed. Watanabe et al. (2011) even state that EBs occur above intergranules. Yet, there is a physically reasonable possibility, which yields reduced continuum contrast at the position of the EB. Considering that EBs occur at faculae with strong magnetic fields, the continuum opacity at the photospheric roots of the fields is strongly modified. The contrasts in Fig. 21b were calculated with the following parameter changes: an increase in the Planck function by an amplitude of $\Delta_{0,B} = 4$ (corresponding to a temperature increase by a factor of 1.56) at $z_i = 300 \text{ km}$ and an increase in line opacity by an amplitude $\Delta_{0,\kappa_{\lambda}} = 5$. In addition, a modification of the continuum opacity in deep layers was introduced as shown in the lower panel of Fig. 20 and with the following parameters: an increase around $z = 100 \text{ km}$ and near the boundaries of x with $\Delta_{\kappa_c} = 3$ and a decrease around the centre of the structure in x by a factor of 2. The reduction of the continuum opacity around the centre of the structure mimics the evacuation within the magnetic structure, while an increase in the opacity on both sides simulates radiative

heating from the hot walls and/or flow of hot material from the reconnection site down along an \cup loop.

Figure 21c depicts the results from inserting parameter variations around the temperature minimum at $z_i = 500 \text{ km}$. An increase in the Planck function does not give much contrast, because this region is transparent to $H\alpha$ photons, the hydrogen level 2 population is very low. The continuum formation is detached from this height, the continuum contrast is small. Only when adding a substantially increased line opacity does one get a contrast similar to what we observed in the bright EBs. The thin dashed contrast curve results from an amplitude $\Delta_{0,\kappa_{\lambda}} = 150$, while we used $\Delta_{0,\kappa_{\lambda}} = 350$ for the thick dashed curve. We consider these opacity changes as reasonable. The temperature and density increase with the latter by a factor up to 3 according to Archontis & Hood (2009), leading to a strong increase of hydrogen in level 2. A more accurate estimate than this zeroth order reasoning is difficult to assess. It requires a non-LTE calculation of radiative transfer in the hydrogen atom at least in two dimensions, which is beyond the scope of the present exploratory modelling.

At $z_i = 500 \text{ km}$, an increase of ε up to $\Delta_{0,\varepsilon} = 350$ also has almost no influence on the contrast (dash-dotted in Fig. 21c, which is almost coincident with the thick dashed contrast curve). With low line opacity, the site is transparent for $H\alpha$ wing photons, and with high line opacity, $H\alpha$ is formed in LTE.

The results from the contrast modelling for the height $z_i = 800 \text{ km}$ are shown in Fig. 21d. While a $\Delta_{0,B} = 7$ again gives only small contrasts, an increase of line opacity with $\Delta_{0,\kappa_{\lambda}} = 50$ is sufficient to strongly increase the contrast. At this height, a sufficiently high hydrogen level 2 density is already present in the background model. An additional increase of ε with $\Delta_{0,\varepsilon} = 150$, possibly from a strongly increased electron density, increases the maximum contrast more to the large value of ~ 2.4 .

An increase of temperature, or Planck function, is needed to produce high contrasts in EBs. Raising only the opacity and collisional control parameter ε leads to *negative* contrasts for heights $z_i = 300 \text{ km}$ and 500 km . This is to be expected, since larger opacity means less contribution from the deep photosphere and intensity formation at larger heights with lower source function. When the opacity and ε increases are placed at $z_i = 800 \text{ km}$, as for Fig. 21d, the line source function has a hump around 900 km . The contrasts are thus positive but small with $C_{\text{EB}} \approx 0.15$, and the intensity increases do not extend beyond $\pm 2 \text{ \AA}$ into the wings of the $H\alpha$ profiles.

4.4.3. Line shifts and asymmetries

Line shifts and asymmetries are produced by velocities and velocity gradients. We show modelled profiles with increasing complexity of the atmospheric dynamics in Fig. 22. As noted above, the intensities around the line minimum are to be taken with a grain of salt, they are partly formed in the low transition region of the model atmosphere. The atmospheric parameters for the simulations are as follows:

1. *Solid profile*: increased B with $\Delta_{0,B} = 7$ and κ_{λ} with $\Delta_{0,\kappa_{\lambda}} = 150$ around T_{min} , which is similar as for the contrast calculations of Fig. 21c above, and upward velocity $v = 5 \text{ km s}^{-1}$ also around T_{min} . This outflow from the heated plasma appears reasonable. It produces a strong blue asymmetry, such that the blue peak in the $H\alpha$ profile is higher than the red peak, as often observed.
2. *Short-dashed profile*: similar to the first point above plus upward velocity of $v = 15 \text{ km s}^{-1}$ in high layers extending

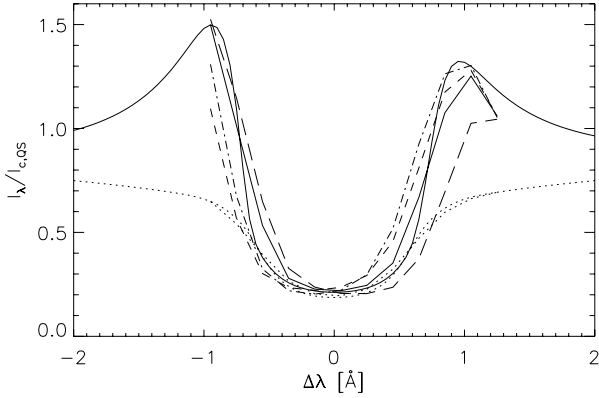


Fig. 22. Modelled line shifts and asymmetries. Smooth solid and dotted profiles extending from -2 \AA to $+2 \text{ \AA}$ are original profiles as calculated, others result from the original profiles taken at positions of $[-0.95, -0.75, \dots, +1.25] \text{ \AA}$ and are smoothed as observed profiles. Dotted: from undisturbed background model FAL P. See text for other profiles, and compare with Fig. 4.

over $\sim 1200 \text{ km}$ in z and 1400 km in x . A blue shift of the absorption profile in high layers also gives the line minimum a blue shift and hides the asymmetry from the upward flow at the site of the EB.

3. *Dash-dotted profile*: similar to the second point above plus reduced Planck function $\Delta_B = -0.3$ and an increased line opacity $\Delta_{0,\kappa_l} = 2$ in high layers. The variations represent a cool, extended cloud above the EB moving towards the observer. It seems that the core of $H\alpha$ has become narrower. Yet, the main effect actually is that the emissions in the $H\alpha$ wings are increased, because the photons are more trapped in deep layers than without the cloud. As a consequence, the source function is increased in high layers (except in the transition region) and the core intensities are higher.
4. *Long-dashed profile*: similar to the third point above but with downward velocity of 15 km s^{-1} and an increased Doppler width in high layers. In this case one may think of a cool, high cloud moving away from the observer. The increase in the Doppler width mimics velocity variations within optically thin elements along the LOS and across the spatial resolution element. The red shift of the absorption profile at high layers introduces a red shift of the line minimum and a stronger blue asymmetry. This behaviour is also seen in the observations (see the discussion on absorbing dark clouds above and the dash-dotted profile in Fig. 5).

We summarise the 2D modelling of $H\alpha$ EBs as follows:

- The heating occurs at heights of $300\text{--}800 \text{ km}$ in the atmosphere. We mention that [Berlicki et al. \(2010\)](#) conclude on a heating height around the temperature minimum of a quiet Sun atmospheric model from their atmospheric modelling. Much lower heights do not reproduce the EB emission in the 1600 \AA UV radiation.
- When modelling the heating at deep photospheric layers, we encountered the problem of producing very high continuum intensities. Heating at photospheric levels of 300 km ($\pm 125 \text{ km}$), which is modelled in Fig. 21 and which can give reasonable $H\alpha_{\text{wing}}$ intensities with a factor of 2.5 higher than from the ambient area, already raises the continuum intensity by a factor of ~ 1.5 . Bright photospheric faculae associated with strong magnetic fields at the EB sites can reach these high intensities, but the intensity increase by heating

in the deep photosphere occurs *in addition* to the facular brightening. The photospheric faculae near EBs are not necessarily the brightest features in the active region.

- Heating at 1000 km and higher produces emissions in the profile around $\pm 0.6 \text{ \AA}$, which do not extend into the wings. This is also not observed.
- An increase in the Planck function at 500 km is not sufficient to produce an $H\alpha$ EB. The absorption from hydrogen level 2 also has to increase by factors of 100 and more. This is because the non-heated atmosphere is transparent to $H\alpha$ photons.
- Line shifts and asymmetries as observed can be modelled by velocities both at the site of the heating and at very high layers.

We have selected parameter variations that reproduce the observed $H\alpha$ profiles, apart from the line minimum intensity. We did not intend to achieve full agreement. The positions and the extent of the variations in the horizontal and vertical direction and their amplitudes are subject to some freedom but not fully arbitrary. We chose reasonable values such as locations in height and size. The occurrence of the modelled $H\alpha$ profiles also in the observed profiles demonstrates the complexity of the dynamics in EBs and their ambient plasma. Uniqueness of parameters to be derived from $H\alpha$ observations cannot be expected. Yet, we are confident that the values of temperature, opacity, collisional excitation (ε), and velocity variations chosen for the modelling are adequate.

5. Conclusions

We studied Ellerman bombs (EBs), or moustaches, by means of time sequences of broadband images at 6300 \AA and in $H\alpha$ and of polarimetric measurements in the Fe I line at 1.6548μ . SDO-HMI and -AIA data also were used. We aimed at high temporal resolution of the order of $1/2 \text{ min}$. With the two-dimensional Triple Etalon Solar Spectrometer (TESOS) we arrived at cadences of 15 s and performed image reconstruction of the broadband and $H\alpha$ time sequences. Scans of the solar image with the Tenerife Infrared Polarimeter II (TIP II) allowed polarimetric measurements with cadences of $28\text{--}46 \text{ s}$, albeit with a small angular extent of $5''\text{--}8''$ in the scan direction. The angular resolution of the broadband images is $0'.40\text{--}0'.45$ and of the narrow-band images in $H\alpha$ is $0'.6\text{--}0'.8$, while the resolution of the IR spectropolarimetric observations is estimated to be $1''\text{--}1'.5$.

Three EBs, identified by the brightness in the line wings of $H\alpha$, were investigated in detail. They were very brilliant with a factor of up to 2.8 brighter than their average neighbourhood. We could follow one of them for more than $1/2 \text{ h}$.

One of the EBs occurred at the outskirts of the penumbra of a complex sunspot in the evolving active region. A two-component magnetic-field fitting revealed opposite polarity fields within the resolution element of $\sim 1''$. Their reconnection may have caused the EB. As seen in AIA data at 1600 \AA and 1700 \AA , flaring continued along a line parallel to this penumbra after we had stopped observing this EB. Another EB showed its brightening close to a strong magnetic field patch and small weak field areas with opposite polarity. Towards the end of its lifetime, this EB had moved into the centre of the strong field patch, where it faded. The third EB showed substantial variations of the close-by magnetic field of opposite polarity with changes of orientation and a decrease of polarimetric signals.

The numerical magneto-hydrodynamic simulations by [Archontis & Hood \(2009\)](#) show that reconnection can take place

at all heights in the solar atmosphere. Yet, our two-dimensional radiative transfer simulations limit the height for the H α EB to ≤ 800 km. For larger heights, narrow emissions at ± 0.6 Å off line centre of H α appear. This is not observed in EBs, the H α line is brightened mostly at ± 0.9 Å and the brightening extends far out into the wings. Wherever the reconnection occurs, the reaction of the H α line is the same with wing brightening.

We consider the temporal resolution of $\sim 1/2$ min of our observations sufficient in view of the longevity of bright EBs. Yet, the polarimetric measurements would profit from higher angular resolution than the $\sim 1''$ achieved here. In addition, larger fields of view than our limited $5''$ – $8''$ should give wider contexts of magnetic fields. More observations closer to disc centre than those used here will also allow one to better distinguish between horizontal and vertical magnetic fields. The combination of high temporal resolution and high angular resolution in large fields of view and with high polarimetric accuracy is demanding. Future solar instrumentation will comply with these needs.

Acknowledgements. We thank Reiner Hammer for his careful reading of the manuscript and for his helpful comments. We are also grateful to Rob Rutten for his knowledgeable refereeing and for his detailed suggestions that helped to greatly improve this paper. N.B.G. acknowledges financial support by Deutsche Forschungsgemeinschaft through grant Schm 1168/9 and by the Senatsausschuss of the Leibniz-Gemeinschaft, Ref.-No. SAW-2012-KIS-5. The work of F.K. was supported by Deutsche Forschungsgemeinschaft through grant KN 152/33. The Vacuum Tower Telescope is operated by the Kiepenheuer-Institut für Sonnenphysik, Freiburg, at the Spanish Observatorio del Teide of the Instituto de Astrofísica de Canarias.

References

- Al, N., Bendlin, C., Hirzberger, J., Kneer, F., & Trujillo Bueno, J. 2004, *A&A*, 418, 1131
- Archontis, V., & Hood, A. W. 2009, *A&A*, 508, 1469
- Auer, L., Fabiani Bendicho, P., & Trujillo Bueno, J. 1994, *A&A*, 292, 599
- Bello González, N., & Kneer, F. 2008, *A&A*, 480, 265
- Bello González, N., Kneer, F., & Puschmann, K. G. 2007, in *Modern Solar Facilities – Adv. Sol. Sci.*, eds. F. Kneer, K. G. Puschmann, & A. D. Wittmann (Universitätsverlag Göttingen), 217
- Bello González, N., Yelles Chaouche, L., Okunev, O., & Kneer, F. 2009, *A&A*, 494, 1091
- Berlicki, A., Heinzel, P., & Avrett, E. H. 2010, *Mem. Soc. Astron. It.*, 81, 646
- Borrero, J. M., Tomczyk, S., Kubo, M., et al. 2011, *Sol. Phys.*, 273, 267
- Bruzek, A. 1968, in *Structure and Development of Solar Active Regions*, ed. K. O. Kiepenheuer, IAU Symp., 35, 293
- Cheung, M. C. M., Schüssler, M., & Moreno-Inertis, F. 2007, *ApJ*, 467, 703
- Cheung, M. C. M., Rempel, M., Title, A. M., & Schüssler, M. 2010, *ApJ*, 720, 233
- Collados, M., Lagg, A., Díaz García, J. J., et al. 2007, in *ASP Conf. Ser.* 368, eds. P. Heinzel, I. Dorotovič, & R. J. Rutten, 611
- de Boer, C. R. 1996, *A&AS*, 120, 195
- Ellerman, F. 1917, *ApJ*, 46, 298
- Fontenla, J. M., Avrett, E. H., & Loeser, R. 1993, *ApJ*, 406, 319
- Georgoulis, M. K., Rust, D. M., & Bernasconi, P. N. 2002, *ApJ*, 575, 506
- Gingerich, O., Noyes, R. W., Kalkofen, W., & Cuny, Y. 1971, *Sol. Phys.*, 18, 347
- Grossmann-Doerth, U., Schüssler, M., & Solanki, S. K. 1988, *A&A*, 206, L37
- Janssen, K. 2003, Ph.D. Thesis, Göttingen university
- Kentischer, T. J., Schmidt, W., Sigwarth, M., & von Uexküll 1998, *A&A*, 340, 569
- Khomenko, E. V., Collados, M., Solanki, S. K., Lagg, A., & Trujillo Bueno, J. 2003, *ApJ*, 408, 1115
- Kitai, R. 1983, *Sol. Phys.*, 87, 135
- Kneer, F. 2010, *Mem. Soc. Astron. It.*, 81, 757
- Kneer, F., & von Uexküll, M. 1991, *A&A*, 247, 556
- Landi Degl'Innocenti, E. 1992, in *Solar Observations: techniques and interpretation*, eds. F. Sánchez, & M. Collados, M. Vázquez (Cambridge: Cambridge University Press), 71
- Leenaarts, J., Rutten, R. J., Sütterlin, P., Carlsson, M., & Uitenbroek, H. 2006, *A&A*, 449, 1209
- Lemen, J. R., Title, A. M., Akin, D. J., et al. 2012, *Sol. Phys.*, 275, 17
- Lin, H. 1995, *ApJ*, 446, 421
- Löfdahl, M., & Scharmer, G. B. 2012, *A&A*, 537, A80
- Maltby P., Avrett, E. H., Carlsson, M., et al. 1986, *ApJ*, 306, 284
- Matsumoto, T., Kitai, R., Shibata, K., et al. 2008, *PASJ*, 60, 577
- Mihalas, D. 1970, *Stellar Atmospheres*, first edn. (San Francisco: Freeman)
- Neckel, H. 1999, *Sol. Phys.*, 184, 421
- Nelson, C. J., Doyle, C., Erdélyi, R., et al. 2013, *Sol. Phys.*, 283, 307
- Ng, K. C. 1974, *J. Chem. Phys.*, 61, 2680
- November, L. J., & Simon, W. G. 1988, *ApJ*, 333, 427
- Pariat, E., Aulanier, G., Schmieder, B., et al. 2004, *ApJ*, 614, 1099
- Pariat, E., Schmieder, B., Berlicki, A., et al. 2007, *A&A*, 473, 279
- Qiu, J., Ding, M. D., Wang, H., Denker, C., & Goode, P. R. 2000, *ApJ*, 544, L157
- Rabin, D. 1992, *ApJ*, 391, 832
- Reardon, K. P., Tritschler, A., & Katsukawa, Y. 2012, *ApJ*, in press
- Rüedi, I., Solanki, S. K., Livingston, W., & Stenflo, J. O. 1992, *A&A*, 263, 323
- Rutten, R. J., Vissers, G. J. M., Rouppe van der Voort, L. H. M., Sütterlin, P., & Vitas, N. 2013, in *Eclipse on the Coral Sea: Cycle 24 Ascending*, eds. P. S. Cally, R. Erdélyi, & A. A. Norton, *J. Phys. Conf. Ser.*, 440, 012007
- Sánchez Almeida, J., Collados, M., & del Toro Iniesta, J. C. 1988, *A&A*, 201, L37
- Sánchez-Andrade Nuño, B., Bello González, N., Blanco Rodríguez, J., Kneer, F., & Puschmann, K. 2008, *A&A*, 486, 577
- Scherrer, P. H., Schou, J., Bush, J. I., et al. 2012, *Sol. Phys.*, 275, 207
- Schlichenmaier, R., & Collados, M. 2002, *A&A*, 381, 668
- Schlichenmaier, R., & Franz, M. 2013, *A&A*, 555, A84
- Severny, A. B. 1956, *Observatory*, 76, 241
- Sheeley, N. R., Jr. 1967, *Sol. Phys.*, 1, 171
- Solanki, S. K., Rüedi, I., & Livingston, W. 1992, *A&A*, 263, 339
- Solanki, S. K., Barthol, P., Danilovic, S., et al. 2010, *ApJ*, 723, L127
- Sütterlin, P. 1998, *A&A*, 333, 305
- Tritschler, A., Schmidt, W., Langhans, K., & Kentischer, T. 2002, *Sol. Phys.*, 211, 17
- von der Lühse, O., & Kentischer, T. J. 2000, *A&AS*, 146, 499
- von der Lühse, O., Soltan, D., Berkefeld, T., & Schelenz, T. 2003, *SPIE*, 4853, 187
- Watanabe, H., Kitai, R., Okamoto, K., et al. 2008, *ApJ*, 684, 736
- Watanabe, H., Vissers, G., Kito, R., Rouppe van der Voort, L., & Rutten, R. J. 2011, *ApJ*, 736, 71